

**DESIGN OF A BIRDCAGE-LIKE RADIO
FREQUENCY TRANSMIT ARRAY COIL
FOR THE MAGNETIC RESONANCE
IMAGING USING EQUIVALENT CIRCUIT
MODEL**

A THESIS SUBMITTED TO
THE GRADUATE SCHOOL OF ENGINEERING AND SCIENCE
OF BILKENT UNIVERSITY
IN PARTIAL FULFILLMENT OF THE REQUIREMENTS FOR
THE DEGREE OF
MASTER OF SCIENCE
IN
ELECTRICAL AND ELECTRONICS ENGINEERING

By
Alireza Sadeghi Tarakameh
May, 2016

Design of a Birdcage-like Radio Frequency Transmit Array Coil for
the Magnetic Resonance Imaging Using Equivalent Circuit Model
By Alireza Sadeghi Tarakameh
May, 2016

We certify that we have read this thesis and that in our opinion it is fully adequate,
in scope and in quality, as a thesis for the degree of Master of Science.

Ergin Atalar(Advisor)

Vakur Behçet Ertürk

Özgür Salih Ergül

Approved for the Graduate School of Engineering and Science:

Levent Onural
Director of the Graduate School

ABSTRACT

DESIGN OF A BIRDCAGE-LIKE RADIO FREQUENCY TRANSMIT ARRAY COIL FOR THE MAGNETIC RESONANCE IMAGING USING EQUIVALENT CIRCUIT MODEL

Alireza Sadeghi Tarakameh

M.S. in Electrical and Electronics Engineering

Advisor: Ergin Atalar

May, 2016

One of the conditions to have a good magnetic resonance (MR) image is applying a homogeneous radio-frequency (RF) excitation (magnetic field) with efficiently high intensity to the region of interest. However, there are some limitations such as specific absorption rate (SAR) which is not allowed to exceed some standard levels. Since SAR level directly depends on the electric field and the electric field is coupled to the magnetic field, there is a trade-off between high-intensity RF-excitation and low SAR level. Moreover, in conventional RF coils (birdcage) for the MRI, the magnetic field profile is almost constant so that its intensity is pretty high at the center of the coil and decreases toward the coil. In such a coil, it is not possible to aim an off-center small region of interest and make the homogeneity concentrated at that region. Transmit array (Tx-array) coils provide high controllability on both electric and magnetic field, so, they would be good solutions for all of these issues, although, they come across the efficiency problem at the center when the same performance of a conventional RF coil is required. This problem has been already handled using a birdcage-like Tx-array coil, however, there are some difficulties to design and tune such a coil.

In this thesis, we proposed a novel design method for birdcage-like Tx-array coil; an eight-channel birdcage-like Tx-array coil is designed using the equivalent lumped-element circuit model. This design profits controllability feature of an array and high transmit efficiency of a birdcage coil at the center, simultaneously. A capacitive decoupling method is utilized in order to get rid of reactive interactions between channels of the array. Then, an optimization (the steepest-descent method) with constraints based on minimizing the electric field and smoothing the magnetic field is applied to the voltage-excitations of the Tx-array coil.

The proposed decoupling method provides 15dB matching for each channel and higher than 12dB decoupling between adjacent channels and at least 19dB for nonadjacent channels. This Tx-array coil provides only 3% less efficiency versus the birdcage coil at the center of the coil, while, at the regions close to the surface of the phantom we achieved more than 72% better efficiency in comparison to the birdcage coil. Furthermore, we demonstrated that the Tx-array is capable to produce a homogeneous magnetic field at an arbitrary (off-center) region of interest. This adjustment can be performed for the electric field as well such that the electric field and so the SAR can be minimized locally.

Consequently, the proposed configuration of the Tx-array coil provides an efficient excitation while capability of local RF shimming and local electric-field-reduction can be achieved.

Keywords: MRI, transmit array, birdcage-like, equivalent circuit, decoupling, RF shimming, SAR reduction, efficient transmit, steepest-descent method.

ÖZET

MANYETİK REZONANS GÖRÜNTÜLEME İÇİN EŞDEĞER DEVRE MODELİ KULLANILARAK KUŞKAFESİ BENZERİ RADYO FREKANS İLETİM DİZİSİ SARGISI TASARIMI

Alireza Sadeghi Tarakameh

Elektrik ve Elektronik Mühendisliği, Yüksek Lisans

Tez Danışmanı: Ergin Atalar

Mayıs, 2016

İyi bir MR görüntüsü elde etmek için koşullardan birisi ilgi bölgesine yüksek yoğunlukta bir homojen radyo frekans (RF) uyarım (manyetik alanı) uygulamaktır. Ancak bazı kısıtlamalar vardır. Örneğin; özel soğrulma oranı (ÖSO) gibi, ve bunun bazı standart seviyeleri geçmemesi gerekmektedir. Bu yüzden yüksek yoğunlukta RF uyarımı ve düşük ÖSO seviyesinin arasında bir değiş tokuş vardır. Üstelik MRG için geleneksel sargıların (kuşkafesi) içerisinde manyetik alanı profili hemen hemen sabittir ve yoğunluk sargının merkezinde en yüksek, kenarlara doğru düşüktür. Böyle bir sargıyla merkezden sapmış, küçük bir ilgi bölgesini hedeflemek ve homojenliği o bölgeye odaklamak mümkün değildir. İletim dizisi sargıları manyetik ve elektrik alanları üzerine yüksek kontrol edebilirlik sağlamaktadırlar. Bu yüzden bu sargılar yukarıda bahsedilmiş sorunlar için iyi bir çözüm olabilir. Ancak bu sargılar kullanıldığında geleneksel RF sargısıyla aynı performansa ihtiyaç duyulduğu zaman, merkezde verimlilik problemiyle karşılaşmaktadır. Bu problem hâlihazırda kuşkafesi benzri iletim dizisi sargısı kullanılarak çözülmüştür. Ancak böyle bir sargının tasarımı ve ayarlaması çeşitli zorluklarla karşılaşmaktadır.

Bu tezde kuşkafesi benzeri iletim dizisi sargısı tasarımı için yeni bir tasarım yöntemi geliştirilmiştir; Eşdeğer yığın eleman devre modeli kullanılarak sekiz kanallı bir kuşkafesi benzeri iletim dizisi sargısı tasarlanmıştır. Bu tasarım bir iletim dizisinin kontrol edilebilirlik özelliği ve bir kuşkafesi sargısının yüksek iletim verimliliği özelliklerinden birlikte yararlanmaktadır. İletim dizisinde kanalların arasındaki reaktif etkileşimi yok etmek için bir kapasitif dekuplaj yöntemi kullanılmaktadır. Daha sonra elektrik alanı minimize etmek ve manyetik alanı

düzeltilmek amaçlı bir optimizasyon yöntemi (en hızlı düşüş yöntemi) iletim dizisinin voltaj uyarımına uygulanmaktadır.

Geliştirilmiş dekoplaaj yöntemi her kanal için 15dB uyumluluk, komşu kanallar arasında 12dB'den fazla ve komşu olmayan kanallar arasında en düşük 19dB dekoplaaj sağlamaktadır. Bu iletim dizisi sargısı kuşkafesi sargısıyla karşılaştırıldığı zaman, sargının merkezinde sadece %3 daha az verimlilik sağlamaktadır, halbuki fantomun yüzeyine yakın olan bir bölgede %72 daha iyi verimlilik elde etmektedir. Ayrıca iletim dizisi rastgele seçilmiş bir bölgede (merkezden sapmış) bir homojen manyetik alanı üretim kabiliyetine sahip olması gösterilmektedir. Bu düzenleme ÖSO'yu bölgesel minimize etmek amacıyla, elektrik alanı içinde uygulanabilmektedir.

Sonuç olarak geliştirilmiş iletim dizisi sargısı verimli uyarım, aynı zamanda bölgesel RF pullama ve ÖSO azaltması kabiliyetine sahip olmaktadır.

Anahtar sözcükler: MRG, iletim dizisi, kuşkafesi benzeri, eşdeğer devre, dekoplaaj, RF pullama, ÖSO azaltması, verimli iletim, en hızlı düşüş yöntemi.

Acknowledgement

First, I would like to express my sincere appreciation to **Prof. Dr. Ergin Atalar** for his wise supervision, endless support and always encouraging me. Also, I would like to thank him for providing us a great research environment at UMRAM. I could not have imagined having a better advisor and mentor for my M.S. study.

Second, I would like to state my deep gratitude to **Prof. Dr. Vakur Behçet Ertürk** and **Prof. Dr. Özgür Salih Ergül** for showing interest in my work and allocating their precious time to read and giving critical comments on this thesis.

I would also like to thank the experts who were involved in the validation survey for this research project: **Taner Demir** and **Umut Gündoğdu**. Without their passionate participation and input, the validation survey could not have been successfully conducted.

I thank my fellow labmates in for the stimulating discussions, for the sleepless nights we were working together before deadlines, and for all the fun we have had in the last two years.

Finally, I must express my very profound gratitude to my parents and to my fiancée, **Ela Gizem**, for providing me with unfailing support and continuous encouragement throughout my years of study and through the process of researching and writing this thesis. This accomplishment would not have been possible without them. Thank you.

Contents

1	Introduction	1
1.1	Motivation	1
1.2	Background	2
1.3	Outline	4
2	Theory and Methods	5
2.1	Calculations of Equivalent Lumped Elements Circuit model for a Band-pass Birdcage Coil and Adjustment of Design Parameters Using Finite-Elements Based Simulations	5
2.1.1	Equivalent Circuit Model for a Band-pass Birdcage Coil with Ignoring the Mutual Inductance Effects	6
2.1.2	Equivalent Circuit Model for a Band-pass Birdcage Coil with Considering the Mutual Inductance Effect	8
2.1.3	Inductance Calculations	10
2.1.4	Resonant Modes and Capacitor Calculations	20
2.1.5	An FEM-Based Optimization	21

2.2	Optimization Using the Steepest-Descent Method	23
2.2.1	Cost Function	24
2.2.2	The Steepest-descent Method	24
2.3	Design of Birdcage-like RF Transmit-Array Coil Using Equivalent Circuit Model and Applying an Optimization Method	27
2.3.1	Design of a Transmit-Array Coil	27
2.3.2	Excitation of the Array	35
3	Experiments and Results	40
3.1	Coil Construction	40
3.2	Shield Construction	42
3.3	Experimental Setup	44
3.4	Resonant Modes	45
3.5	Coupling Between Channels	46
3.6	Homogeneity	49
3.7	Field Efficiency	54
3.8	Local B_1^+ Shimming	56
3.9	Local Electric-field-reduction	56
4	Discussion	58

5 Conclusion

List of Figures

2.1	Demonstration of a band-pass birdcage coil as a schematic model (a), and equivalent lumped-element circuit model (b).	6
2.2	Schematic demonstration of a 2-port band-pass birdcage coil.	7
2.3	Schematic demonstration of a 2-port band-pass birdcage coil.	9
2.4	Cross-sections of two nearby conductor strips such that the short edges (a) or long edges (b) are parallel. In this configuration, it is assumed that the current is flowing in the indicated direction, inside the cross-sections.	11
2.5	Demonstration of two rungs as two parallel equal strips.	14
2.6	Demonstration of two adjacent end-ring segments as two equal strips meeting at end points.	15
2.7	Demonstration of two nonadjacent end-ring segments as two equal strips in the same plane without intersection.	16
2.8	Configuration of end-ring segments and their end-points' distances which are used in mutual inductance calculations.	17
2.9	Demonstration of two segments of the different end-rings as two equal strips in the different planes.	18

2.10	Cross-sectional demonstration of the coil, RF shield, and the electrical image of the coil.	19
2.11	Configuration of end-ring segments on the coil and its image.	20
2.12	Electric field profile inside a birdcage coil while it is excited in linear mode (one-port excitation).	22
2.13	Magnetic field (a) and electric field (b) profile inside a birdcage coil while it is excited in quadrature mode (two-port excitation with 90° phase difference).	23
2.14	Operational algorithm of the steepest-descent method.	26
2.15	Planer view of three adjacent loops of the array coil.	29
2.16	Equivalent circuit model of the three adjacent loops of the array coil.	30
2.17	Single copper loop inside the RF shield. (a) Modal demonstration, (b) Equivalent circuit model.	31
2.18	Equivalent circuit model of three adjacent loops of the array coil considering the load effect.	32
2.19	Block diagram model of an N-port network (a) with N-excitation (b).	36
3.1	Constructed 8-channel birdcage-like Tx-array coil.	40
3.2	Simulated Tx-array Structure using ANSYS HFSS v15.	41
3.3	Constructed two-port head birdcage coil to compare with Tx-array coil.	42
3.4	Constructed RF shield used in MR-experiment.	43

3.5	8-channel T/R-switched used in MR-experiment in order to make using the the array coil as transceiver coil possible.	44
3.6	Nickel Chloride Hexahydrate solution used as a phantom for imaging.	44
3.7	Demonstration of tuning and matching for the birdcage coil in simulation (a) and measurement (b).	45
3.8	Demonstration of tuning and matching for the Tx-array coil in simulation (a) and measurement (b).	46
3.9	Demonstration of coupling between channel no.1 and adjacent channels in the Tx-array. (a) Channel 2, (b) Channel 8.	46
3.10	S-parameters, related to channel 1.	47
3.11	Graphical demonstration of S-matrix for the Tx-array.	48
3.12	B_1^+ -map inside the phantom produced by each individual channel of the Tx-array coil in simulation (a) and MR-experiment (b). The features of the MR-experiment are: TR = 8.6s, TE = 6ms, NEX = 1, 128×128 , FOV = 20cm, and slice thickness = 5mm.	49
3.13	A demonstration for individual channels excitation in a MR-experiment, (a) B_1^+ -map, (b) MR-image. The MR-images in (b) are acquired using a gradient echo (GRE) pulse sequence (TR = 100s, TE = 4ms, NEX = 4, 128×128 , FOV = 20cm, and slice thickness = 5mm.	50
3.14	CP excitation inside the phantom and B_1^+ -maps corresponding to simulation of the birdcage coil (a), simulation of the Tx-array (b), and MR-experiment of the Tx-array (c). Corresponding MR-image using the Tx-array (d). The MR-image is acquired using a GRE pulse sequence (TR = 100s, TE = 10ms, NEX = 1, 128×128 , FOV = 20cm, slice thickness = 5mm, and flip angle = 79.5°). . .	51

3.15	Distribution of B_1^+ on transversal axes for the birdcage coil (a) and Tx-array coil (b).	52
3.16	Distribution of normalized B_1^+ on transversal circles with radii of 1cm, 3cm, 5cm, 7cm, and 9cm for the birdcage coil (a) and Tx-array coil (b); and relative standard deviation of B_1^+ on transversal circles for both birdcage and Tx-array coil.	53
3.17	Demonstration of B_1^+ -map inside the phantom produced by (a) a quadrature-excited birdcage coil and (b) the Tx-array that is optimized without consideration of SAR. Electric field demonstration for the corresponding (c) birdcage, and (d) Tx-array coil.	54
3.18	Demonstration of efficiency-map inside the phantom produced by (a) a quadrature-excited birdcage coil, and (b) the Tx-array that is optimized to achieve high efficiency at a region close to surface of the phantom.	55
3.19	An arbitrary B_1^+ excited inside the phantom by the Tx-array coil. (a) The expected B_1^+ -map, (b) The achieved B_1^+ -map.	56
3.20	(a) The electric field distribution corresponding to CP excitation of a birdcage coil, (b) The goal electric field with off-center minimum, and (c) The optimized electric field corresponding to the Tx-array.	57

List of Tables

2.1	Values of $\ln k$ that contributes in Eq. 2.12 for the arrangement shown in Fig. 2.4a.	12
2.2	Values of $\ln k$ that contributes in Eq. 2.12 for the arrangement shown in Fig. 2.4b.	13
2.3	Values of $\ln e$ that contributes in Eq. 2.13 for the arrangements shown in Fig. 2.4a and Fig. 2.4b.	14
3.1	Capacitor values on the array coil, used in simulation and experiment.	42
3.2	B_1^+ efficiency comparison between the birdcage coil and the Tx-array. All values are related to the center of the phantom.	55

Chapter 1

Introduction

1.1 Motivation

Producing highly homogeneous excitation inside the imaging object during the MRI usually has been considered as a critical issue. In spite of achieving acceptable homogeneity radio-frequency (RF) magnetic field using standard birdcage coil [1], local RF-shimming is still an interesting area [2–4] that needs some improvements. In shimming applications, achieving more degree of freedom provides more controllability on magnetic field profile inside the coil [5]. Therefore, using a multi-channel transmit-array coil can be a good idea to achieve this capability.

Furthermore, birdcage coil has a very high power efficiency with remarkable magnetic field homogeneity inside a big volume of interest [1, 6], compared to other RF-transmit coils; thus, birdcage-like transmit array coil [7] benefits from the special structure of birdcage coil. In addition to that, its higher degree of freedom provides more controllability on the performance of the coil such that, it would produce a high-efficiency RF-excitation at regions close to the surface of the phantom where the efficiency of the conventional birdcage coil crucially decreases.

Moreover, favorable magnetic field profile inside the imaging object may be changed, occasionally. For instance, in cardiac imaging applications, though we need high-intensity magnetic field on the cardiac of patient [8, 9], birdcage coil excites the center of the coil with the highest efficiency and it decays toward the edges of the coil. Local RF-shimming can have such an advantage so that one can consume most of the power to produce a high-intensity homogeneous excitation within a small region of interest while the region is off-center of the coil [10].

Multichannel Tx-array coil can be also investigated in the sense of specific absorption rate (SAR) reduction. Since SAR is defined as the dissipated power inside the body due to flowing the electric current within a conductive media [2], reducing the electric field inside the body causes the SAR reduction. Although there are some methods to modify the electric field produced by the conventional RF transmit coil [11, 12], Tx-array coils may play a significant role in this issues while they provide a high controllability on both electric and magnetic field. In other words, optimizing the voltage-excitations of the Tx-array coil in such a way that reduces the electric field while enhances the magnetic field will perform as both local RF shimming and local SAR reduction, simultaneously [13, 14].

1.2 Background

In spite of the advantages of using Tx-array coil for the MRI, the design and manufacturing of such coils is a significant challenge due to the mutual coupling between coils of the array [15, 16].

In classical Tx-array design, overlapping decoupling [17–19] is used in order to omit the reactive interaction between elements of the array coil. This method is based on the concept that the direction of magnetic field producing by a single conducting loop is inverse inside and outside the loop, consequently, overlapping two loops in proper locations can eliminate the reactive effect of the loops on each other. This provides a broadband decoupling between two adjacent loops, however, finding the exact and appropriate locations for the loops is an important

and challenging issue since the decoupling is highly sensitive to the correct amount of overlapping. One disadvantage of using array coil which consists of overlapping loops in comparison to a conventional birdcage coil is the difficulty of producing a homogeneous excitation with high efficiency inside the region of interest. In other words, this kind of Tx-array coil provides a low performance in comparison to a birdcage coil in the typical MRI applications when the region of interest is located at the center of the RF-coil. Another disadvantage of this method of design comes to the picture if the array coil has also receiving functionality such that to make the complex sensitivity of phased-array coils sufficiently distinct in parallel spatially-encoded MRI, it is desirable to have no overlapping between coils [20]. Also, this method does not determine any solution for the coupling issue between nonadjacent coils.

In some work, capacitive decoupling is utilized to eliminate the coupling effect between the adjacent coils [9,21–24]. In this method, one or several capacitors are used between the adjacent coils to eliminate the effect of the mutual inductance between them. In such a design, they tried to sustain the shape of the birdcage coil the same in order to achieve the same performance of the birdcage coil when the region of the interest is at the center of the coil. Although this design meets the requirements to produce the same magnetic field profile with the birdcage coil, it still does not achieve the efficiency of the birdcage coil possibly due to the twice amount of copper strips used in rungs in comparison to the birdcage coil. This extra amount of copper causes extra dissipated power which is supposed to be consumed inside the imaging object. Furthermore, the decoupling is still very sensitive to the value of the capacitor and also the decoupling is not satisfied in a broad band but for a single frequency. This method also does not provide any extra alternative for nonadjacent coils.

Another design solved the coupling issue for nonadjacent coils using inductive decoupling [25–27]. They used a transformer between two coils to produce a mutual inductance between them, opposite to the existing mutual inductance between two coils. This design also resolves the frequency band problem and provides a broadband decoupling. Furthermore they achieved the magnetic field distribution similar to the one that the birdcage coil produces. This is because of

the similar shape of their coil to shape of the birdcage coil. However, the efficiency problem remains the same probably due to the extra power loss on copper strips of the rungs.

1.3 Outline

In Chapter 2, the birdcage coil and its performance is briefly introduced. Then an equivalent lumped elements circuit model for such a coil is presented. This circuit consists of many inductances due to the strips of the coil. These inductances include all self and mutual ones and we tried to consider and calculate all of them. In coil design also some capacitors are used in combination with the mentioned inductors in order to generate some resonant modes. Furthermore, an optimization method is expressed in detail in order to calculate the proper capacitor values for producing the desirable resonant modes. Subsequently, the similar method is used for designing the birdcage-like Tx-array coil. This design includes tuning, decoupling, and exciting the coil.

In Chapter 3, construction of the coil and its RF-shield is described, moreover, the results consisting of the S-parameters, B_1^+ -map, and MR-images are presented. The S-parameters are proof-of-concept for decoupling and tuning method which we used. In addition B_1^+ -map and MR-images show the highly homogeneous magnetic field is excited inside the Nickel Chloride Hexahydrate solution phantom. Also, the results of the Tx-array coil are compared to the results of a home-made birdcage coil such that the similar efficiency to the birdcage coil is achieved. Eventually, the optimization method presented in Chapter 2 is used in order to reduce the SAR and shim the RF field locally.

In Chapter 4, some defects of our coil and some limitations in the design are described, also, future improvements and future applications are discussed.

Finally, in Chapter 5, results and expectations of this work are recited.

Chapter 2

Theory and Methods

In this chapter, the main idea of the design method of the birdcage-like Tx-array coil is discussed. Indeed, the essential point in this design is to utilize the equivalent circuit model in a correct manner, in other words, it is so critical to model the effect of all parameters involved in the coil as an appropriate lumped element in the equivalent circuit model. Also, an optimization method is presented that is utilized in various phases of this design.

2.1 Calculations of Equivalent Lumped Elements Circuit model for a Band-pass Birdcage Coil and Adjustment of Design Parameters Using Finite-Elements Based Simulations

In this section, the fundamental theory of the birdcage coil [28] is re-presented since the same structure is utilized in the birdcage-like Tx-array coil.

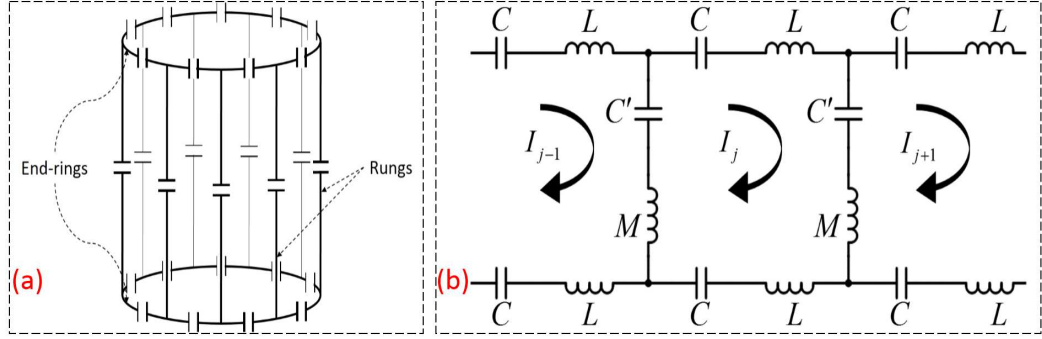


Figure 2.1: Demonstration of a band-pass birdcage coil as a schematic model (a), and equivalent lumped-element circuit model (b).

2.1.1 Equivalent Circuit Model for a Band-pass Birdcage Coil with Ignoring the Mutual Inductance Effects

A band-pass birdcage coil schematically can be shown as Fig. 2.1a. By modeling each wire or strip as an inductor (this assumption is valid only if the wavelength is much larger than strips' sizes), the equivalent circuit model for a band-pass birdcage coil can be shown as Fig. 2.1b which is explained in details by Jin et al. [29]. As a simplification, at the beginning, they assumed that mutual inductances between all strips can be neglected (the effect of mutual inductances is taken into account in section 2.1.2). In Fig. 2.1b, L and M represent the self-inductances of end-ring segments and rungs, respectively. Therefore, Kirchhoff's voltage law inside the j^{th} loop can be written as Eq. 2.1.

$$\begin{aligned}
 & j\omega M(I_j - I_{j-1}) + j\omega M(I_j - I_{j+1}) + 2j\omega L I_j - \frac{2j}{\omega C} I_j + \frac{j}{\omega C'}(I_{j-1} + I_{j+1}) = 0 \\
 & j = 1, \dots, N \\
 & \rightarrow 2 \left(L + M - \frac{1}{\omega^2 C} - \frac{1}{\omega^2 C'} \right) I_j - \left(M - \frac{1}{\omega^2 C'} \right) (I_{j-1} + I_{j+1}) = 0 \quad j = 1, \dots, N
 \end{aligned} \tag{2.1}$$

Where N is the number of loops existing in Fig. 2.1a. Since the configuration must satisfy the periodicity condition, $I_{j+N} = I_j$, therefore, N linearly independent solutions exist for Eq. 2.1 as follows

$$(I_j)_m = \begin{cases} \cos \frac{2\pi m j}{N} & m = 0, 1, \dots, N/2 \\ \sin \frac{2\pi m j}{N} & m = 1, 2, \dots, N/2 - 1 \end{cases} \tag{2.2}$$

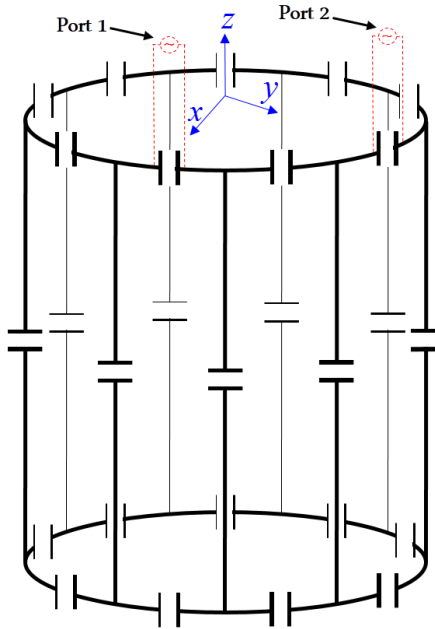


Figure 2.2: Schematic demonstration of a 2-port band-pass birdcage coil.

Consequently, the current on the j^{th} rung of the coil can be expressed as

$$(I_j)_m - (I_{j-1})_m = \begin{cases} -2 \sin \frac{\pi m}{N} \sin \frac{2\pi m(j-\frac{1}{2})}{N} & m = 0, 1, \dots, N/2 \\ 2 \sin \frac{\pi m}{N} \cos \frac{2\pi m(j-\frac{1}{2})}{N} & m = 1, 2, \dots, N/2 - 1 \end{cases} \quad (2.3)$$

Considering the solution corresponding to $m = 1$ bounds the rungs to have a current distribution like $\sin \phi$ or $\cos \phi$ (dependent on the position of the excitation). Value of m denotes the resonant-mode number.

Accordingly, assume a birdcage coil with two excitation ports on the upper end-ring as shown in Fig. 2.2. Note that the first port has placed on the x-axis and the second port is on the y-axis. If only the first port gets been excited (linear excitation), observable from Eq. 2.2, the current distribution on the end-rings at the first mode ($m = 1$) will be similar $\cos \phi$ so that leads to a $\sin \phi$ -like current distribution on the rungs. Therefore, this case can be assumed similar to the cylindrical surface current $\hat{a}_z J_0 \sin \phi$ discussed in [29] and the case can be considered as a solution of the Laplace equation for a scalar magnetic potential (assuming quasi-static condition) that leads to a magnetic field within the coil as follows

$$\bar{B}_1 = \hat{a}_x \frac{\mu_0 J_0}{2} \quad (2.4)$$

Obviously, an excitation on the second port provides a current distribution like $\hat{a}_z J_0 \cos \phi$ which creates a magnetic field inside the coil as follows

$$\bar{B}_2 = \hat{a}_y \frac{\mu_0 J_0}{2} \quad (2.5)$$

Now, it is enough to consider the excitation on both ports simultaneously and applying 90° phase difference to the second one (quadrature excitation). Using the superposition theorem the total magnetic field inside the coil can be obtained as follows

$$B_{total} = \bar{B}_1 + j\bar{B}_2 = \frac{\mu_0 J_0}{2} (\hat{a}_x + j\hat{a}_y) \quad (2.6)$$

Manifestly, this is the expected homogeneous circularly polarized RF magnetic field which can be produced by the birdcage coil with quadrature excitation when it is operating in the first resonant mode.

2.1.2 Equivalent Circuit Model for a Band-pass Birdcage Coil with Considering the Mutual Inductance Effect

Since the structure used in birdcage-like Tx-array coil is the same with a band-pass birdcage coil, the same equivalent circuit model and the same formulas can be utilized. Therefore, in this section, it has been tried to take all feasible effects into account and then derive a general formulation for such a structure.

The equivalent circuit model of birdcage coil shown in Fig. 2.1b can be rearranged as Fig. 2.3.

Following definitions can be done related to the circuit model in Fig. 2.3.

- $L_{j,j}$: Self-inductance of the end-ring segment in j^{th} loop
- $L_{j,k}$: Mutual inductance between end-ring segments in j^{th} and k^{th} loops on the same end-ring
- $\tilde{L}_{j,k}$: Mutual inductance between end-ring segments in j^{th} and k^{th} loops on the different end-rings

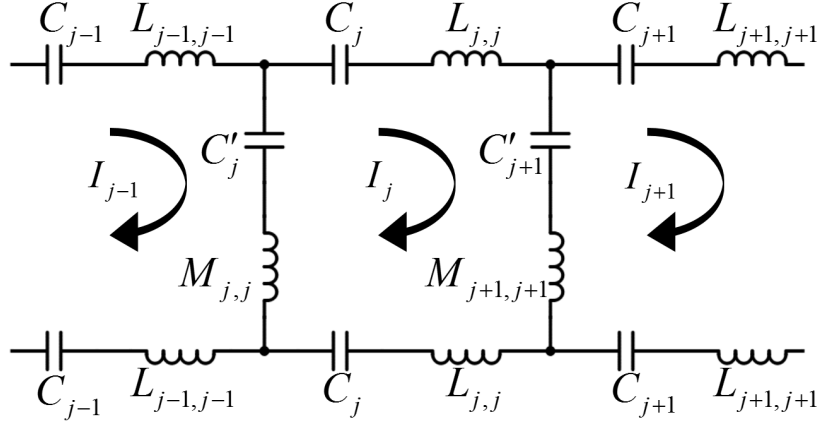


Figure 2.3: Schematic demonstration of a 2-port band-pass birdcage coil.

- $M_{j,j}$: Self-inductance of the j^{th} rung
- $M_{j,k}$: Mutual inductance between j^{th} and k^{th} rungs

Note that it is too difficult to show the mutual inductances in Fig. 2.3 but they are considered in calculations. Considering definitions above, the Kirchhoffs voltage law for the j^{th} loop can be written as

$$\begin{aligned}
& 2 \left(j\omega L_{j,j} I_j + j\omega \sum_{\substack{k=1 \\ k \neq j}}^N L_{j,k} I_k - j\omega \sum_{k=1}^N \tilde{L}_{j,k} I_k \right) - \frac{2j}{\omega C} I_j - \frac{2j}{\omega C'} I_j + \frac{j}{\omega C'} (I_{j-1} + I_{j+1}) \\
& + j\omega M_{j,j} (I_j - I_{j-1}) + j\omega \sum_{\substack{k=1 \\ k \neq j}}^N M_{j,k} (I_k - I_{k-1}) + j\omega M_{j+1,j+1} (I_j - I_{j+1}) \\
& + j\omega \sum_{\substack{k=1 \\ k \neq j+1}}^N M_{j+1,k} (I_{k-1} - I_k) = 0 \quad j = 1, \dots, N \\
& \Rightarrow 2j \sum_{k=1}^N (L_{j,k} - \tilde{L}_{j,k}) I_k + j \left[\sum_{k=1}^N (M_{j,k} - M_{j+1,k}) I_k - \sum_{k=1}^N (M_{j,k} - M_{j+1,k}) I_{k-1} \right] \\
& - \frac{2j}{\omega^2} \left(\frac{1}{C} + \frac{1}{C'} \right) I_j + \frac{j}{\omega^2 C'} (I_{j-1} + I_{j+1}) = 0 \quad j = 1, \dots, N \\
& \Rightarrow \sum_{k=1}^N \left[M_{j,k} - M_{j+1,k} - M_{j,k+1} + M_{j+1,k+1} + 2(L_{j,k} - \tilde{L}_{j,k}) \right] I_k \\
& = \frac{1}{\omega^2} \left[2 \left(\frac{1}{C} + \frac{1}{C'} \right) I_j - \frac{1}{C'} I_{j-1} - \frac{1}{C'} I_{j+1} \right] \quad j = 1, \dots, N
\end{aligned} \tag{2.7}$$

This can be rearranged in the form of a matrix equation as follows [29]

$$\bar{K} \cdot \bar{I} = \frac{1}{\omega^2} \bar{H} \cdot \bar{I} \tag{2.8}$$

Where \bar{I} denotes a vector consist of mesh current of each loop shown in Fig. 2.3. Moreover, elements of matrices \bar{K} and \bar{H} can be represented as

$$K_{j,k} = M_{j,k} - M_{j+1,k} - M_{j,k+1} + M_{j+1,k+1} + 2(L_{j,k} - \tilde{L}_{j,k}) \quad (2.9)$$

$$H_{j,k} = 2\delta_{j,k} \left(\frac{1}{C} + \frac{1}{C'} \right) - \frac{1}{C'} (\delta_{j,k-1} + \delta_{j,k+1}) \quad (2.10)$$

Where $\delta_{j,k}$ is the Kronecker delta defined as

$$\delta_{j,k} = \begin{cases} 1 & j = k \\ 0 & j \neq k \end{cases} \quad (2.11)$$

2.1.3 Inductance Calculations

The main difficulty of inductance calculation is solving the field integrals and evaluating them on some arbitrary geometries as well. This problem has already been solved for some commonly-used geometries using the geometrical mean distance (GMD) theory [30] and corresponding tables .

Geometrical Mean Distance

There are some close formulas for self-inductance of a single straight wire and also for mutual inductance between two straight wires [31] in any feasible situation. Since all strips on the birdcage coil can be represented as integration of many straight wires, so the inductance values somehow can be expressed as total interaction between these wires.

GMD implies the distance that two wires should be placed from each other in order to act like the original problem of interest from the inductance point of view. In other words, the original problem of calculation of inductances of a birdcages strips simply turns to inductance calculations of straight wires using GMD.

Geometrical mean distance for two strips can be calculated using the following

formula [32]

$$\ln R = \ln p + \ln k \quad (2.12)$$

Where p is the distance between centers of strips cross-sections and k is a unitless parameters that values of $\ln k$ are given in Table 2.1 [32] and Table 2.2 [32] for two commonly used configurations shown in Fig. 2.4a and Fig. 2.4b, respectively.

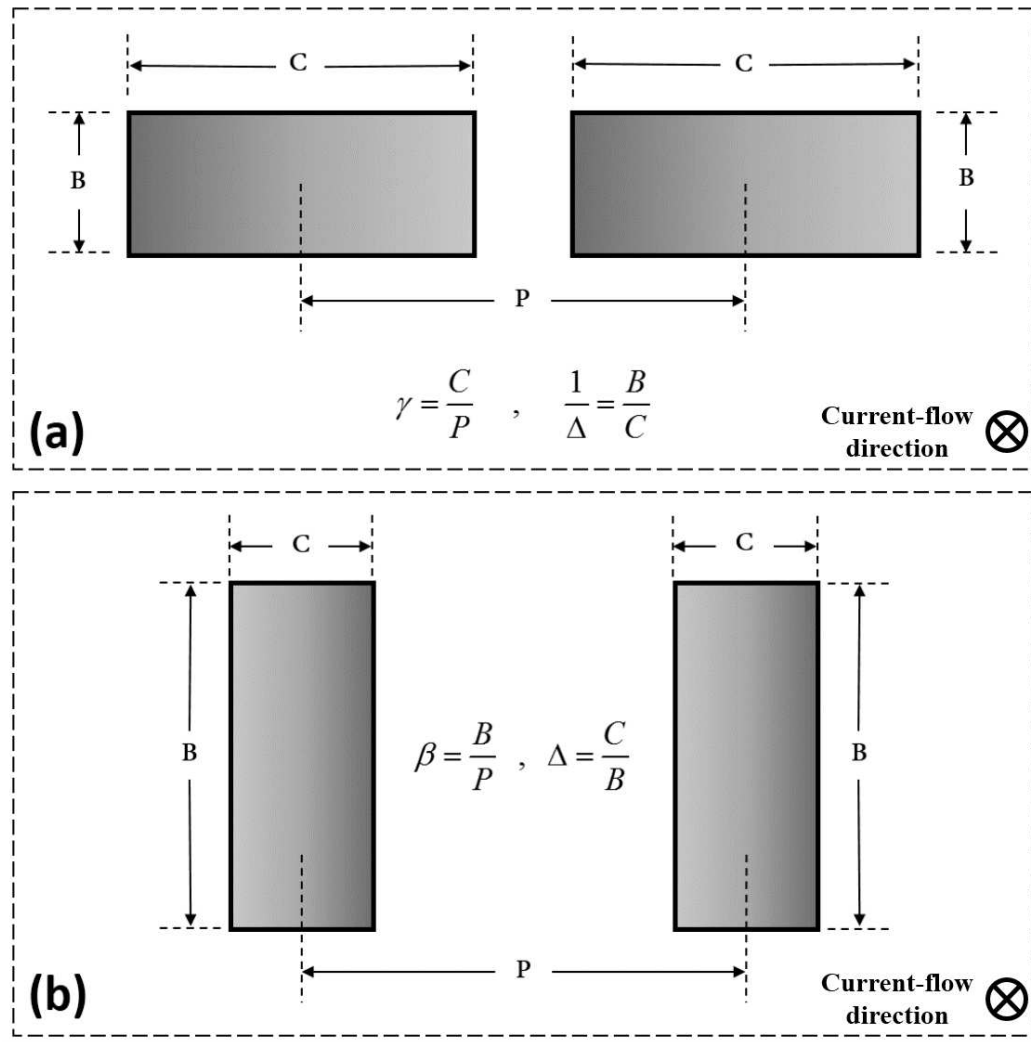


Figure 2.4: Cross-sections of two nearby conductor strips such that the short edges (a) or long edges (b) are parallel. In this configuration, it is assumed that the current is flowing in the indicated direction, inside the cross-sections.

γ	$\frac{1}{\Delta} = 0$	$\frac{1}{\Delta} = 0.1$	$\frac{1}{\Delta} = 0.2$	$\frac{1}{\Delta} = 0.3$	$\frac{1}{\Delta} = 0.4$	$\frac{1}{\Delta} = 0.5$
0	0	0	0	0	0	0
0.05	-0.0002	-0.0002	-0.0002	-0.0002	-0.0002	-0.0002
0.1	0.0008	0.0008	0.0008	0.0008	0.0007	0.0006
0.15	0.0019	0.0019	0.0018	0.0017	0.0016	0.0014
0.2	0.0034	0.0033	0.0032	0.003	0.0028	0.0025
0.25	-0.0053	-0.0052	-0.0051	-0.0048	-0.0044	-0.0039
0.3	0.0076	0.0076	0.0073	0.0069	0.0064	0.0057
0.35	0.0105	0.0104	0.01	0.0095	0.0087	0.0078
0.4	0.0138	0.0136	0.0132	0.0125	0.0115	0.0102
0.45	0.0176	0.0174	0.0169	0.0159	0.0146	0.013
0.5	-0.022	-0.0217	-0.021	-0.0198	-0.0182	-0.0161
0.55	0.0269	0.0268	0.0257	0.0243	0.0222	0.0197
0.6	0.0325	0.0321	0.031	0.0292	0.0267	0.0235
0.65	0.0388	0.0383	0.0369	0.0347	0.0316	0.0277
0.7	0.0458	0.0452	0.0435	0.0408	0.037	0.0325
0.75	-0.0536	-0.0529	-0.0509	-0.0476	-0.0431	-0.0375
0.8	0.0625	0.0616	0.0591	0.0551	0.0497	0.0431
0.85	0.0725	0.0714	0.0683	0.0634	0.0569	0.0491
0.9	0.0839	0.0825	0.0786	0.0726	0.0648	0.0555
0.95	0.0973	0.0954	0.0903	0.0828	0.0734	0.0625
1	-0.1137	-0.1106	-0.1037	-0.0942	-0.0828	-0.07

Table 2.1: Values of $\ln k$ that contributes in Eq. 2.12 for the arrangement shown in Fig. 2.4a.

Self-inductances

Self-inductance of a straight strip can be simply expressed in the following closed-formula [32]

$$L = 0.2l \left(\ln \frac{2l}{B+C} + 0.5 - \ln e \right) \quad (2.13)$$

Where the constant coefficient 0.2 has unit of $\mu H/cm$, l is the length of the strip in cm , B and C are thickness and width of the strip, respectively (in cm). Obviously, the resultant inductance value, L , has unit of μH . Values for $\ln e$ are given in Table 2.3 in terms of B/C . In dealing with very thin strips used in birdcage coil the ratio of B/C is almost zero and according to Table 2.3 [32], $\ln e$ can be taken zero.

β	$\Delta = 0$	$\Delta = 0.1$	$\Delta = 0.2$	$\Delta = 0.3$	$\Delta = 0.4$	$\Delta = 0.5$
0	0	0	0	0	0	0
0.1	0.0008	0.0008	0.0008	0.0008	0.0007	0.0006
0.2	0.0033	0.0033	0.0032	0.003	0.0028	0.0025
0.3	0.0074	0.0073	0.0071	0.0067	0.0062	0.0056
0.4	0.0129	0.0128	0.0124	0.0118	0.0109	0.0098
0.5	0.0199	0.0197	0.0191	0.0182	0.0169	0.0152
0.6	0.0281	0.0278	0.0271	0.0258	0.024	0.0216
0.7	0.0374	0.0371	0.0351	0.0344	0.032	0.029
0.8	0.0477	0.0473	0.0451	0.044	0.0411	0.0373
0.9	0.0589	0.0584	0.0559	0.0544	0.0506	0.0464
1	0.0708	0.0702	0.0685	0.0655	0.0614	0.056
$\frac{1}{\beta}$	$\Delta = 0$	$\Delta = 0.1$	$\Delta = 0.2$	$\Delta = 0.3$	$\Delta = 0.4$	$\Delta = 0.5$
0.9	0.0847	0.0841	0.0821	0.0787	0.0738	0.0675
0.8	0.1031	0.1023	0.0999	0.0959	0.0903	0.0829
0.7	0.1277	0.1268	0.124	0.1192	0.1125	0.1037
0.6	0.1618	0.1607	0.1573	0.1507	0.1436	0.1329
0.5	0.2107	0.2094	0.02053	0.1984	0.1886	0.1754
0.4	0.2843	0.2826	0.2776	0.2691	0.2567	
0.3	0.4024	0.4003	0.3942	0.3831		
0.2	0.6132	0.6105	0.6021			
0.1	1.0787	1.1075				

Table 2.2: Values of $\ln k$ that contributes in Eq. 2.12 for the arrangement shown in Fig. 2.4b.

According to Fig. 2.3 and the definitions provided in section 2.1.2 and utilizing the Eq. 2.13, self-inductance of the j^{th} rung can be obtained as follows

$$M_{rung} = 0.2l_{rung} \left(\ln \frac{2l_{rung}}{w_{rung}} + 0.5 \right) \quad (2.14)$$

Similarly, self-inductance of the end-ring segment in j^{th} loop can be represented in the following formula

$$L_{ER} = 0.2l_{ER} \left(\ln \frac{2l_{ER}}{w_{ER}} + 0.5 \right) \quad (2.15)$$

In Eq. 2.14 and Eq. 2.15, w_{rung} and w_{ER} are width of rungs and end-rings, respectively. Also, l_{rung} and l_{ER} denote corresponding lengths where l_{ER} can be calculated as follows for an N-rung birdcage coil with radius of R_{coil}

$$l_{ER} = \frac{2\pi R_{coil}}{N} \quad (2.16)$$

B/C or C/B	$\ln e$	B/C or C/B	$\ln e$
0	0	0.5	0.00211
0.025	0.00089	0.55	0.00203
0.05	0.00146	0.6	0.00197
0.1	0.0021	0.65	0.00192
0.15	0.00239	0.7	0.00187
0.2	0.00249	0.75	0.00184
0.25	0.00249	0.8	0.00181
0.3	0.00244	0.85	0.00179
0.35	0.00236	0.9	0.00178
0.4	0.00228	0.95	0.00177
0.45	0.00219	1	0.00177

Table 2.3: Values of $\ln e$ that contributes in Eq. 2.13 for the arrangements shown in Fig. 2.4a and Fig. 2.4b.

Mutual Inductances

All cases for mutual inductance calculations in birdcage coil can be represented as mutual inductance between two straight filaments with considering the GMD concept.

• Rungs

Since all rung strips are parallel to each other, two equal length parallel straight filaments will be a good modeling as shown in Fig. 2.5. Eq. 2.17 [32] represents the corresponding mutual inductance value between j^{th} and k^{th} rungs.

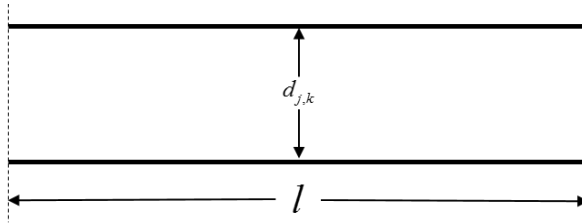


Figure 2.5: Demonstration of two rungs as two parallel equal strips.

$$M_{j,k} = 0.2l_{rung} \left[\ln \left(\frac{l_{rung}}{d_{j,k}} + \sqrt{1 + \frac{l_{rung}^2}{d_{j,k}^2}} \right) - \sqrt{1 + \frac{d_{j,k}^2}{l_{rung}^2}} + \frac{d_{j,k}}{l_{rung}} \right] \quad (2.17)$$

Where $d_{j,k}$ denotes the GMD between j^{th} and k^{th} rungs that can be calculated using Fig. 2.4a or Fig. 2.4b according to their positions.

- **End-rings**

For two adjacent end-ring segments, the model of equal filaments meeting at a point presented in Fig. 2.6 is very reasonable with considering the GMD value.

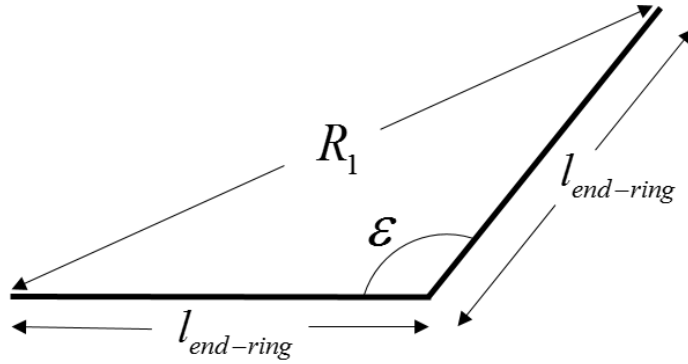


Figure 2.6: Demonstration of two adjacent end-ring segments as two equal strips meeting at end points.

Eq. 2.18 and Eq. 2.19 [32] give the intersection angle and the mutual inductance value related to this case, respectively.

$$\cos \epsilon = 1 - \frac{R_1^2}{2l_{ER}^2} \quad (2.18)$$

$$L_{j,k}^{k=j+1} = 0.4l \cos \epsilon \tanh^{-1} \left(\frac{l_{ER}}{l_{ER} + R_1} \right) \quad (2.19)$$

where GMD value will take place of R_1 .

Similarly, it is appropriate to use equal filaments in the same plane and not meeting in order to model nonadjacent end-ring segments on the same end-ring. The model is represented in Fig. 2.7 and corresponding formulas are given in Eq. 2.20-2.25 [32].

$$\alpha^2 = R_4^2 - R_3^2 + R_2^2 - R_1^2 \quad (2.20)$$

$$m = l = l_{ER} \quad (2.21)$$

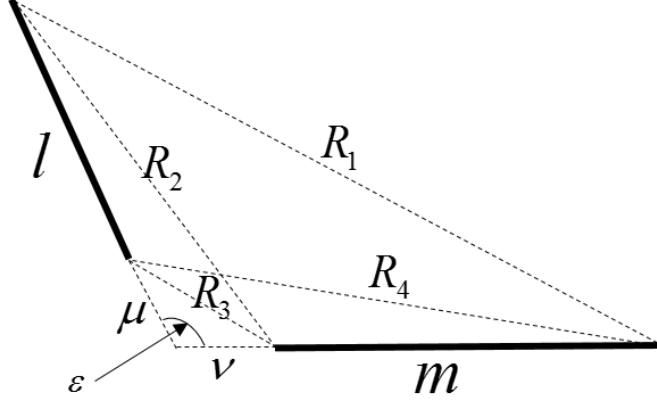


Figure 2.7: Demonstration of two nonadjacent end-ring segments as two equal strips in the same plane without intersection.

$$\cos \varepsilon = \frac{\alpha^2}{2ml} \quad (2.22)$$

$$\mu = \frac{[2m^2(R_2^2 - R_3^2 - l^2) + \alpha^2(R_4^2 - R_3^2 - m^2)]l}{4m^2l^2 - \alpha^4} \quad (2.23)$$

$$\nu = \frac{[2l^2(R_4^2 - R_3^2 - m^2) + \alpha^2(R_2^2 - R_3^2 - l^2)]m}{4m^2l^2 - \alpha^4} \quad (2.24)$$

$$\begin{aligned} L_{j,k}^{j,k} &= 0.2 \cos \varepsilon \left[(\mu + l) \tanh^{-1} \left(\frac{m}{R_1^{j,k} + R_2^{j,k}} \right) + (\nu + m) \tanh^{-1} \left(\frac{l}{R_1^{j,k} + R_4^{j,k}} \right) \right. \\ &\quad \left. - \mu \tanh^{-1} \left(\frac{m}{R_3^{j,k} + R_4^{j,k}} \right) - \nu \tanh^{-1} \left(\frac{l}{R_2^{j,k} + R_3^{j,k}} \right) \right] \end{aligned} \quad (2.25)$$

where $R_1 - R_4$ are distances between end-points of two segments that are shown in Fig. 2.8 and they should be determined case-wise as follows

$$R_1^{j,k} = 2R_{coil} \left| \sin \left(\frac{\theta_{k+1} - \theta_j}{2} \right) \right| \quad (2.26)$$

$$R_2^{j,k} = 2R_{coil} \left| \sin \left(\frac{\theta_k - \theta_j}{2} \right) \right| \quad (2.27)$$

$$R_3^{j,k} = 2R_{coil} \left| \sin \left(\frac{\theta_k - \theta_{j+1}}{2} \right) \right| \quad (2.28)$$

$$R_4^{j,k} = R_2^{j,k} \quad (2.29)$$

where

$$\theta_j = \left(\frac{j-1}{N} \right) 2\pi \quad (2.30)$$

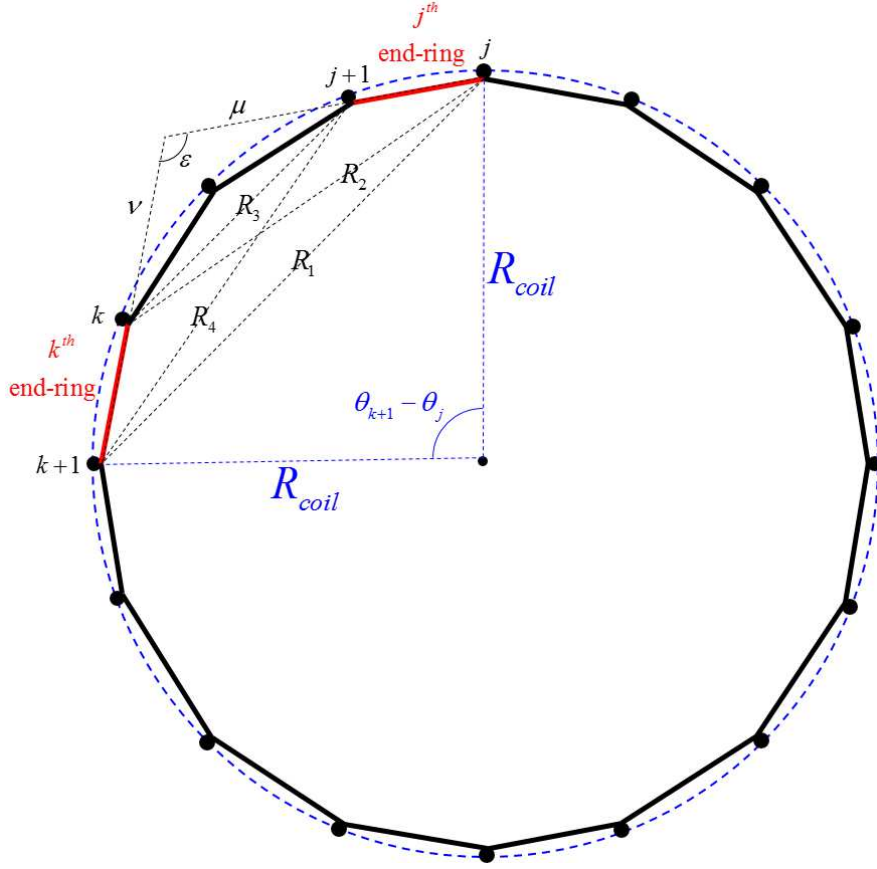


Figure 2.8: Configuration of end-ring segments and their end-points' distances which are used in mutual inductance calculations.

Calculation of mutual inductance between two segments of the different end-rings has the same procedure with the previous case however the proper model is two straight filaments placed in different planes as shown in Fig. 2.9. A formula for the corresponding mutual inductance is given in Eq. 2.31 [32].

$$\begin{aligned} \tilde{L}_{j,k} = 0.2 \cos \varepsilon \left[(\mu + l) \tanh^{-1} \left(\frac{m}{\tilde{R}_1^{j,k} + \tilde{R}_2^{j,k}} \right) + (\nu + m) \tanh^{-1} \left(\frac{l}{\tilde{R}_1^{j,k} + \tilde{R}_4^{j,k}} \right) \right. \\ \left. - \mu \tanh^{-1} \left(\frac{m}{\tilde{R}_3^{j,k} + \tilde{R}_4^{j,k}} \right) - \nu \tanh^{-1} \left(\frac{l}{\tilde{R}_2^{j,k} + \tilde{R}_3^{j,k}} \right) \right] - \frac{\Omega d}{\sin \varepsilon} \end{aligned} \quad (2.31)$$

where

$$\Omega = \tan^{-1} \left[\frac{d^2 \cos \varepsilon + (\mu + l)(\nu + m) \sin^2 \varepsilon}{d \tilde{R}_1^{j,k}} \right] \quad (2.32)$$

and d denotes the distance between planes of two filaments but in this case must be replaced with GMD value. Consequently, end-points distances can be

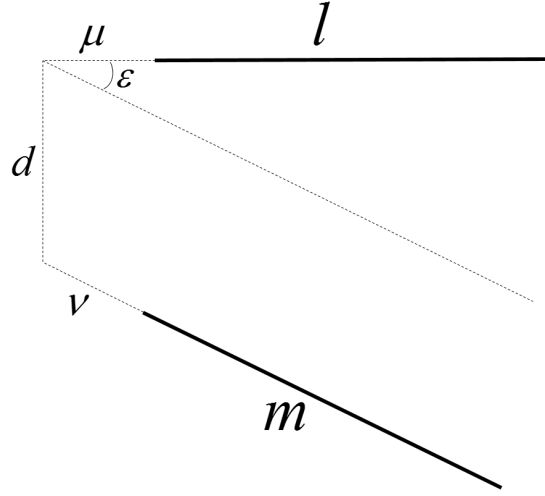


Figure 2.9: Demonstration of two segments of the different end-rings as two equal strips in the different planes.

determined using Eq. 2.26 - 2.29 as follows

$$\tilde{R}_m^{j,k} = \sqrt{(R_m^{j,k})^2 + d^2} \quad m = 1, \dots, 4 \quad (2.33)$$

• Shielding Effects

RF-shield inside an MRI system is responsible for eliminating all radio frequency EM-waves existing around and they may cause some significant effects inside the coil. Also, this shield prevents the wave produced by RF-coil to leak out of the coil, in other words, it sustains all RF wave inside the coil. These Shield-effects appear as mutual inductances in the equivalent circuit model. In order to calculate the mutual inductance value coming from shields conductor, it is reasonable to use image theory and model the shield as surface currents on a conductor similar to the RF-coil but a radius of R_{image} shown in Fig. 2.10. Value of R_{image} is given in Eq. 2.34 which is a direct result of image theory.

$$R_{image} = \frac{R_{shield}^2}{R_{coil}} \quad (2.34)$$

Therefore, the image of the shield can be assumed similar to the original coil so that it has its own rungs and rings. On the other hand, the mutual inductance between this image and the birdcage coil can be calculated utilizing the appropriate formulas (Eq. 2.17, 2.25, and 2.31) expressed in section 2.1.3.

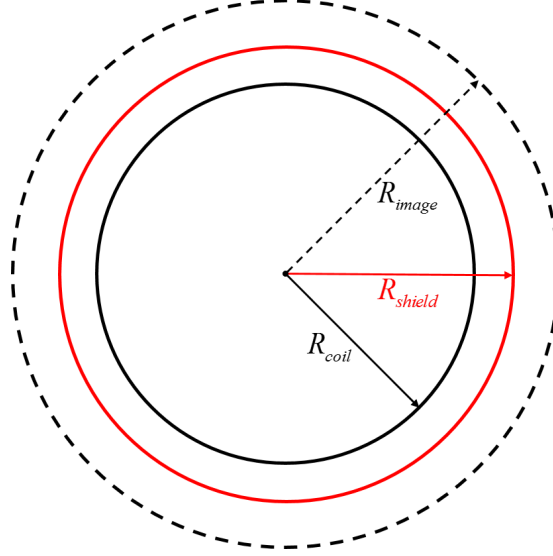


Figure 2.10: Cross-sectional demonstration of the coil, RF shield, and the electrical image of the coil.

Assume that $L'_{j,k}$ denotes mutual inductance between end-ring segments in j^{th} and k^{th} loops on the same end-rings of the coil and its image. Then using the model provided in Fig. 2.7 the mutual inductance can be obtained as follows

$$L'_{j,k} = 0.2 \cos \varepsilon \left[(\mu + l') \tanh^{-1} \left(\frac{m}{R'_1{}^{j,k} + R'_2{}^{j,k}} \right) + (\nu + m) \tanh^{-1} \left(\frac{l'}{R'_1{}^{j,k} + R'_4{}^{j,k}} \right) - \mu \tanh^{-1} \left(\frac{m}{R'_3{}^{j,k} + R'_4{}^{j,k}} \right) - \nu \tanh^{-1} \left(\frac{l'}{R'_2{}^{j,k} + R'_3{}^{j,k}} \right) \right] \quad (2.35)$$

where $R'_1 - R'_4$ are shown in Fig. 2.11 and the values are calculated in Eq. 2.36-2.40.

$$R'_1{}^{j,k} = \sqrt{R_{coil}^2 + R_{image}^2 - 2R_{coil}R_{image} \cos(\theta_{k+1} - \theta_j)} \quad (2.36)$$

$$R'_2{}^{j,k} = \sqrt{R_{coil}^2 + R_{image}^2 - 2R_{coil}R_{image} \cos(\theta_k - \theta_j)} \quad (2.37)$$

$$R'_3{}^{j,k} = \sqrt{R_{coil}^2 + R_{image}^2 - 2R_{coil}R_{image} \cos(\theta_k - \theta_{j+1})} \quad (2.38)$$

$$R'_4{}^{j,k} = \sqrt{R_{coil}^2 + R_{image}^2 - 2R_{coil}R_{image} \cos(\theta_{k+1} - \theta_{j+1})} \quad (2.39)$$

$$l' = \frac{R_{shield}}{R_{coil}} l_{ER} \quad (2.40)$$

Similarly, $\tilde{L}'_{j,k}$ is defined as mutual inductance between end-ring segments in j^{th} and k^{th} loops on the different end-rings of the coil and its image. The model in

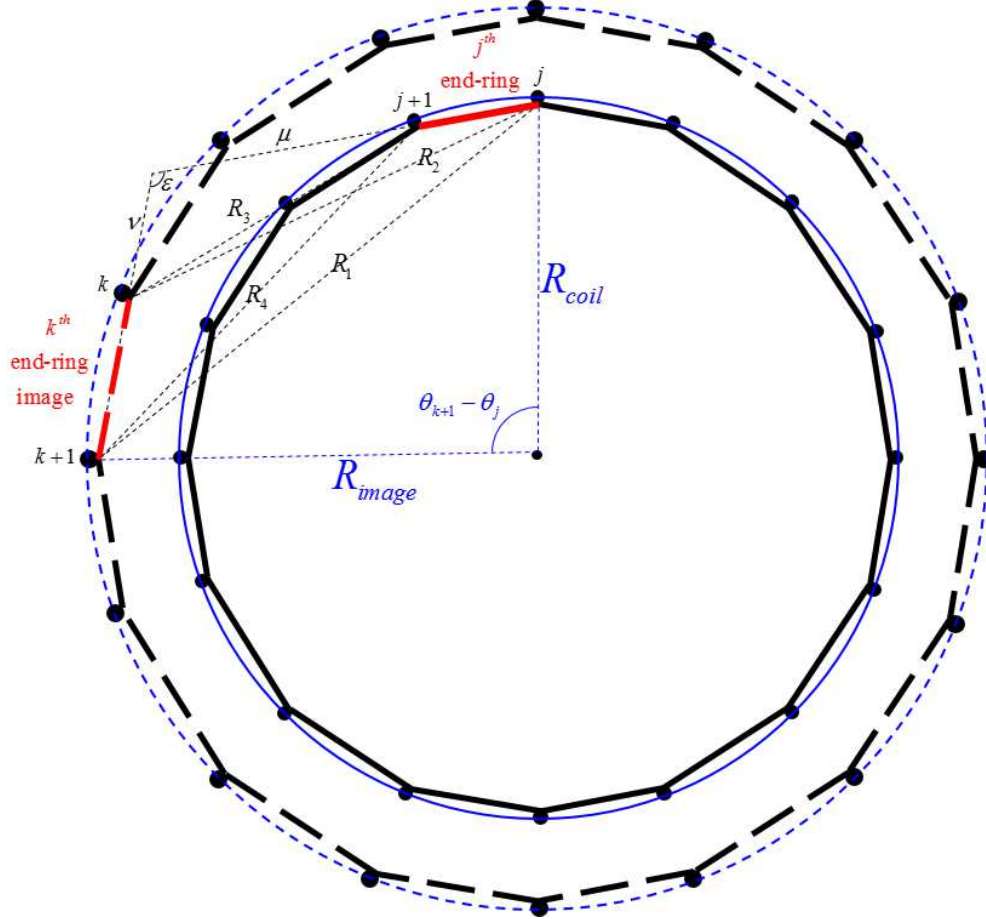


Figure 2.11: Configuration of end-ring segments on the coil and its image.

Fig. 2.9 can be used for calculations and the result is

$$\begin{aligned} \tilde{L}'_{j,k} = & 0.2 \cos \varepsilon \left[(\mu + l) \tanh^{-1} \left(\frac{m}{\tilde{R}'_1{}^{j,k} + \tilde{R}'_2{}^{j,k}} \right) + (\nu + m) \tanh^{-1} \left(\frac{l}{\tilde{R}'_1{}^{j,k} + \tilde{R}'_4{}^{j,k}} \right) \right. \\ & \left. - \mu \tanh^{-1} \left(\frac{m}{\tilde{R}'_3{}^{j,k} + \tilde{R}'_4{}^{j,k}} \right) - \nu \tanh^{-1} \left(\frac{l}{\tilde{R}'_2{}^{j,k} + \tilde{R}'_3{}^{j,k}} \right) \right] - \frac{\Omega' d}{\sin \varepsilon} \end{aligned} \quad (2.41)$$

where

$$\tilde{R}'_m{}^{j,k} = \sqrt{(R'_m{}^{j,k})^2 + d^2} \quad m = 1, \dots, 4 \quad (2.42)$$

2.1.4 Resonant Modes and Capacitor Calculations

According to the equivalent circuit model in section 2.1.2(Fig 2.3), an N-rung birdcage coil has N resonant modes and the first mode ($m = 1$) is the desired

mode to operate as RF-coil in MRI. This criterion is used in design process of a birdcage coil. When the coil is performing in the first mode, the mesh currents inside each loop can be expressed as Eq. 2.2. Furthermore, Eq. 2.8 is relating the current distributions inside the loops and the circuit lumped-elements. Since the vector \bar{I} for the desired mode is defined in Eq. 2.3 as the first resonant mode of the birdcage coil ($m = 1$) and also the elements of matrix \bar{K} in Eq. 2.8 can be calculated using the methods in section 2.1.3, choosing a feasible value for C' then solving a simple equation for C leads to the desired capacitor value for a band-pass birdcage coil. Choosing j^{th} row of the matrix equation in Eq. 2.8 gives

$$C = \left[\omega^2 \left(\sum_{k=1}^N K_{j,k} \frac{I_k}{I_j} \right) + \frac{1}{2C'} \left(\frac{I_{j-1} + I_{j+1} - 2I_j}{I_j} \right) \right]^{-1} \quad (2.43)$$

Note that in order to take the shielding effects to account, it is enough to replace $L_{j,k}$ with $L_{j,k} - L'_{j,k}$, $\tilde{L}_{j,k}$ with $\tilde{L}_{j,k} - \tilde{L}'_{j,k}$, and $M_{j,k}$ with $M_{j,k} - M'_{j,k}$ in Eq. 2.9. Once capacitor values found by the mentioned method, Eq. 2.8 can be investigated in terms of resonant modes. In order to have a nontrivial solution for Eq. 2.8, the determinant of $\left[\bar{K} - \frac{1}{\omega^2} \bar{H} \right]$ must be zero. Since $\left[\bar{K} - \frac{1}{\omega^2} \bar{H} \right]$ is an $N - by - N$ matrix, its determinant is a polynomial from degree of N , therefore, N solutions or in other word N different modes will be obtained.

On the other hand, neither the coil resistance nor the resistance coming from the load is considered in this formulation, however, it is taken into account in section 2.3.

2.1.5 An FEM-Based Optimization

In the method provided in section 2.1.4, it has been tried to have as much precision as possible however there are still some approximations used so that contribute some errors to the problem. For instance, calculated inductance values are not hundred-percent accurate and also the resistive effects are not considered. These errors reduce the accuracy in calculation of the desirable capacitor values. In order to decrease these errors, some electromagnetic (EM) optimization can be applied to the problem.

Finite-element method (FEM)-based EM simulations are commonly used to model the real-life structures. Therefore, optimization of the capacitor values using EM-simulator can significantly reduce the contributing errors. The frequency of the first resonant mode can be taken as the main criterion of the optimization. In the other hand, the type of the MR scanner (strength of the B_0), used for the design of RF-coil, determines the desired RF resonant frequency. Resonant modes of a birdcage coil can be obtained directly from the frequency domain spectrum of S-parameters of the coil that can be extracted from EM simulations. Then, tuning the first resonant mode to the target frequency is taken as the goal of optimization. Current distribution profile can be utilized as a criterion in order to diagnose the first resonant mode between all resonant modes. According to Eq. 2.3 and Eq. 2.4, only one mode causes the current distribution similar to the birdcages desired one, therefore that mode should be taken as the first mode.

Looking at the magnetic field and electric field distribution inside the coil can determine the first resonant mode as well. The electric field profile due to a linear excitation on x-axis at the desirable mode inside the birdcage coil should be similar to Fig. 2.12 [33].

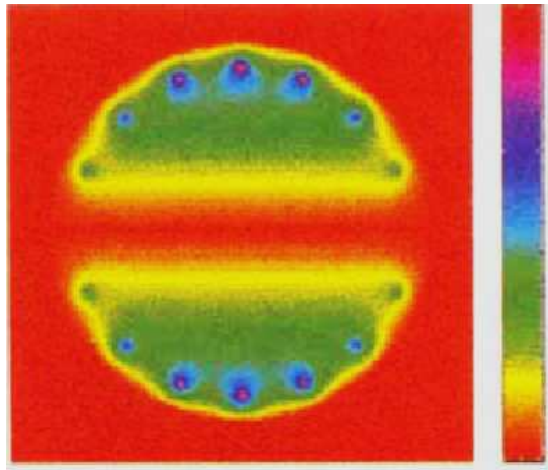


Figure 2.12: Electric field profile inside a birdcage coil while it is excited in linear mode (one-port excitation).

The optimization comes to the picture by sweeping the capacitor values while S_{11} spectrum of both ports are been taken as the criterion of the optimization.

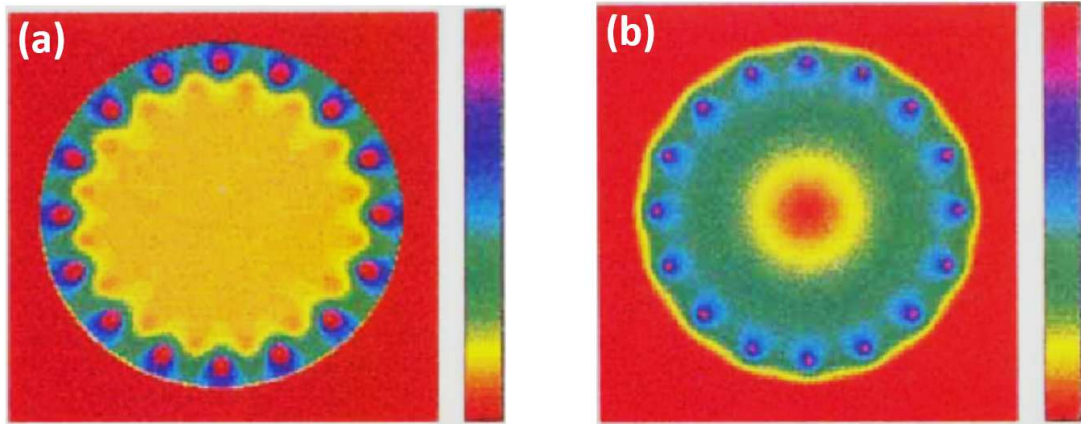


Figure 2.13: Magnetic field (a) and electric field (b) profile inside a birdcage coil while it is excited in quadrature mode (two-port excitation with 90° phase difference).

Eventually, in order to validate the optimization results, the coil should be derived using quadrature excitation at the first resonant mode then the field distributions shown in Fig. 2.13a [33] and Fig. 2.13b [33] should be observed for B-field and E-field, respectively.

2.2 Optimization Using the Steepest-Descent Method

In design-based problems one may come across an inverse problem which means that the desirable solutions are available or well-known thus corresponding design parameters should be investigated [34]. RF-coil parameters can be a sensible instance where the desired current distributions or field profiles are well-known. Such an inverse problem can be thought as an optimization problem that a minimization method should be applied to the mismatch between target solution and the solution comes from predicted design.

2.2.1 Cost Function

The cost function can be defined as a criterion of total mismatch between ultimate solution and the solution due to initial guess. The mismatches can be defined piecewise as follows

$$\bar{e}(\bar{x}) = \begin{bmatrix} e_1(\bar{x}) \\ \vdots \\ e_N(\bar{x}) \end{bmatrix} = \begin{bmatrix} S_1(\bar{x}) - S_1^{goal} \\ \vdots \\ S_N(\bar{x}) - S_N^{goal} \end{bmatrix} \quad (2.44)$$

$$\bar{x} = \begin{bmatrix} x_1 & \dots & x_M \end{bmatrix}^T \quad (2.45)$$

Where $\bar{e}(\bar{x})$ denotes the vector of residual error such that its elements are defined as the mismatch between each elements of the target solution and predicted solution. \bar{S} vector in Eq. 2.44 stands for the solution and \bar{x} represents model vector consists of required design parameters. In order to solve a minimization problem, it will be a good idea to gather the effects of all errors in a single parameter (cost function) as follows

$$C(\bar{x}) = |\bar{e}(\bar{x})|^2 = \sum_{i=1}^N |e_i(\bar{x})|^2 = \sum_{i=1}^N |S_i(\bar{x}) - S_i^{goal}|^2 \quad (2.46)$$

Therefore, minimizing the cost function leads to the minimum error vector which occurs when the desirable design parameters are achieved. A bunch of minimization approaches are available, however we preferred to employ the steepest-descent method which is based on a local quadratic model of the cost function.

2.2.2 The Steepest-descent Method

In some common cases minimization methods deal with large matrix inversions, therefore we utilized an iterative method [35] to avoid this numeric issue. The quadratic model of cost function can be made up using the first three terms of the Taylor-series expansion of the cost function as follows

$$C(\bar{x}_k + \bar{p}_k) \approx C(\bar{x}_k) + \bar{g}^T(\bar{x}_k) \cdot \bar{p}_k + \frac{1}{2} \bar{p}_k^T \cdot \bar{G}(\bar{x}_k) \cdot \bar{p}_k \quad (2.47)$$

where \bar{x}_k is the model vector in the k^{th} iteration and accordingly \bar{p}_k denotes the step of \bar{x}_k toward the minimum of the cost function.

$\bar{g}(\bar{x})$ and $\bar{G}(\bar{x})$ are the gradient vector (first order derivative) and Hessian matrix (second order derivative) of the cost function, respectively and can be determined by the following expressions

$$\bar{g}(\bar{x}) = \nabla C(\bar{x}) = \left[\frac{\partial C}{\partial x_1} \quad \dots \quad \frac{\partial C}{\partial x_M} \right]^T = \text{Re} \left\{ \bar{J}^T(\bar{x}) \cdot \bar{e}(\bar{x}) \right\} \quad (2.48)$$

$$\bar{G}(\bar{x}) = \nabla \nabla C(\bar{x}) = \begin{bmatrix} \frac{\partial^2 C}{\partial x_1^2} & \dots & \frac{\partial^2 C}{\partial x_M \partial x_1} \\ \vdots & \ddots & \vdots \\ \frac{\partial^2 C}{\partial x_1 \partial x_M} & \dots & \frac{\partial^2 C}{\partial x_M^2} \end{bmatrix} = \text{Re} \left\{ \bar{J}^T(\bar{x}) \cdot \bar{J}(\bar{x}) \right\} \quad (2.49)$$

where x_i is the i^{th} component of the model vector, and $\bar{J}(\bar{x})$ is the Jacobian matrix which is defined as follows

$$\bar{J}(\bar{x}) = \begin{bmatrix} \frac{\partial e_1}{\partial x_1} & \dots & \frac{\partial e_1}{\partial x_M} \\ \vdots & \ddots & \vdots \\ \frac{\partial e_N}{\partial x_1} & \dots & \frac{\partial e_N}{\partial x_M} \end{bmatrix} = \begin{bmatrix} \frac{\partial S_1}{\partial x_1} & \dots & \frac{\partial S_1}{\partial x_M} \\ \vdots & \ddots & \vdots \\ \frac{\partial S_N}{\partial x_1} & \dots & \frac{\partial S_N}{\partial x_M} \end{bmatrix} \quad (2.50)$$

According to Eq. 2.48 and Eq. 2.49, the only calculation burden is to obtain the Jacobian matrix. Then some simple matrix multiplications come to the picture which is not a big deal in aspect of calculation difficulties.

Generally, determining the Jacobian matrix needs some numerical calculations. In order to calculate the derivative in each element of the Jacobian matrix, finite-difference method can be utilized as follows

$$J_{i,j} = \frac{\partial S_i}{\partial x_j} \approx \frac{S_i(\bar{x} + \delta x_j) - S_i(\bar{x})}{\delta x_j} \quad (2.51)$$

$S_i(\bar{x} + \delta x_j)$ denotes the i^{th} component of the systems solution when a very small perturbation in j^{th} component of the model vector \bar{x} is occurred. In order to solve the minimization problem using this method, step vector \bar{p}_k in each iteration must be calculated and then the model vector \bar{x}_k should be updated by \bar{p}_k . The simple argument of the steepest-descent method [36] is to choose the search direction along the negative of the gradient vector (Eq. 2.52). This guarantees to move toward the minimum in each iteration.

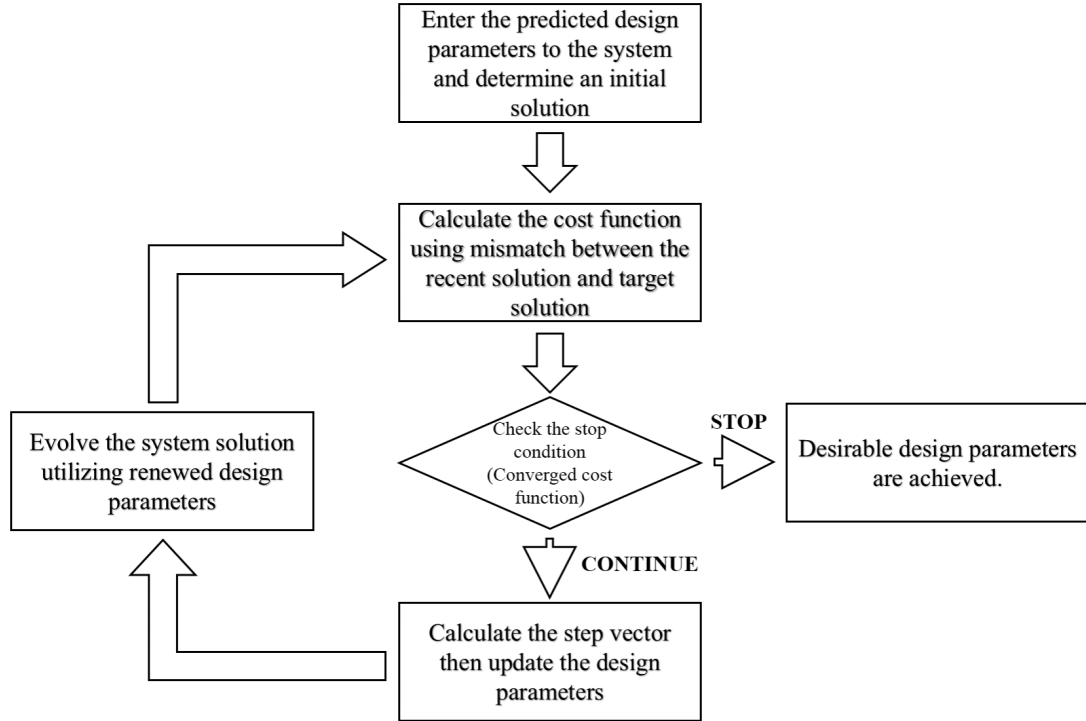


Figure 2.14: Operational algorithm of the steepest-descent method.

$$\bar{p}_k = -\gamma_k \bar{g}(\bar{x}) = -\gamma_k \bar{g}_k \quad (2.52)$$

In Eq. 2.52, vector $-\bar{g}(\bar{x})$ and γ_k denote search-step directions and lengths, respectively. In order to achieve the minimum as fast as possible, step sizes must be chosen such that the reduction in cost function get maximized. Substituting Eq. 2.52 into Eq. 2.47 gives

$$C(\bar{x}_k + \bar{p}_k) \approx C(\bar{x}_k) - \gamma_k |\bar{g}_k|^2 + \frac{1}{2} \gamma_k^2 \bar{g}_k^T \cdot \bar{G}(\bar{x}) \cdot \bar{g}_k \quad (2.53)$$

In order to obtain the minimum of the left-hand side in Eq. 2.53, derivative of the right-hand side with respect to γ_k should be taken and make the result zero as follows

$$-|\bar{g}_k|^2 + \gamma_k \bar{g}_k^T \cdot \bar{G}(\bar{x}) \cdot \bar{g}_k = 0 \rightarrow \gamma_k = \frac{|\bar{g}_k|^2}{\bar{g}_k^T \cdot \bar{G}(\bar{x}) \cdot \bar{g}_k} \quad (2.54)$$

Substituting Eq. 2.54 into Eq. 2.53 gives

$$\bar{p}_k = -\frac{|\bar{g}_k|^2}{\bar{g}_k^T \cdot \bar{G}(\bar{x}) \cdot \bar{g}_k} \bar{g} \quad (2.55)$$

which is used to update the model vector \bar{x} in k^{th} iteration.

Algorithm of this iterative minimization method briefly can be expressed as the diagram shown in Fig. 2.14.

2.3 Design of Birdcage-like RF Transmit-Array Coil Using Equivalent Circuit Model and Applying an Optimization Method

In this section, an equivalent circuit model, very similar to the one in section 2.1.2, is presented for the birdcage-like Tx-array coil and then the optimization method discussed in section 2.2 is utilized to calculate the desirable components of the equivalent circuit. The same optimization method is also used to excite each channel in order to achieve the aim of this thesis based on efficiency enhancement and SAR reduction.

2.3.1 Design of a Transmit-Array Coil

In design of a birdcage-like Tx-array coil, decoupling between the channels, tuning to the desirable frequency, and impedance matching of the input ports can be considered as the most essential parameters.

Decoupling of the Channels

EM coupling between channels of an array would be problematic from two point of views

- The input power from amplifier on one port may go out into the amplifier on the other port. This may cause some significant damages on the internal circuits

of the amplifier.

- The input power at one port is supposed to be transmitted to the imaging tissue, however coupling may cause some power transformation between ports and consequently power loss on the port terminations.

Therefore, decoupling of all channels from each other turns to an important issue. One commonly used decoupling method is capacitive decoupling which is based on the concept that the EM coupling between two loops is occurred because of the magnetic flux passes through a loop due to the electric current on the other one. This can be modeled as mutual inductances in the equivalent circuit. Obviously, every inductive effect can be canceled using a proper capacitive component at a desirable frequency. In this design procedure, one of the assumptions have been made is that the coupling between nonadjacent loops (channels) are negligible, so the coupling between adjacent loops with a common rung is supposed to vanish using an appropriate capacitor on the common rung.

Fig. 2.15 shows the objective part of the structure so that the loop in the middle (j^{th} loop) is supposed to be decoupled from $(j - 1)^{th}$ and $(j + 1)^{th}$ loops.

The equivalent circuit model for such a structure is already offered in section 2.1.2. Accordingly, Fig. 2.16 can be a reasonable equivalent circuit model for the structure shown in Fig. 2.15.

The Kirchhoffs voltage law inside the first loops leads to

$$\begin{aligned}
& j\omega \left\{ 2 \left[(L_{j,j} - L'_{j,j}) I_j - (\tilde{L}_{j,j} - \tilde{L}'_{j,j}) I_j + (L_{j,j-1} - L'_{j,j-1}) I_{j-1} \right. \right. \\
& \quad \left. \left. - (\tilde{L}_{j,j-1} - \tilde{L}'_{j,j-1}) I_{j-1} + (L_{j,j+1} - L'_{j,j+1}) I_{j+1} - (\tilde{L}_{j,j+1} - \tilde{L}'_{j,j}) I_{j+1} \right] \right. \\
& \quad + (M_{j,j} - M'_{j,j}) (I_j - I_{j-1}) + (M_{j,j-1} - M'_{j,j-1}) I_{j-1} \\
& \quad - (M_{j,j+1} - M'_{j,j+1}) (I_j - I_{j+1}) - (M_{j,j+2} - M'_{j,j+2}) I_{j+1} \\
& \quad \left. + (M_{j+1,j+1} - M'_{j+1,j+1}) (I_j - I_{j+1}) - (M_{j+1,j-1} - M'_{j+1,j-1}) I_{j-1} \right. \\
& \quad \left. - (M_{j+1,j} - M'_{j+1,j}) (I_j - I_{j-1}) + (M_{j+1,j+2} - M'_{j+1,j+2}) I_{j+1} \right\} \\
& \quad - \frac{j}{\omega} \left[2 \left(\frac{1}{C_j^d} \right) I_j + \left(\frac{1}{C_j^d} + \frac{1}{C_{j+1}^d} \right) I_j - \frac{1}{C_j^d} I_{j-1} - \frac{1}{C_{j+1}^d} I_{j+1} \right] = 0
\end{aligned} \tag{2.56}$$

All self- and mutual inductances are defined the same as definitions in section 2.1.2.

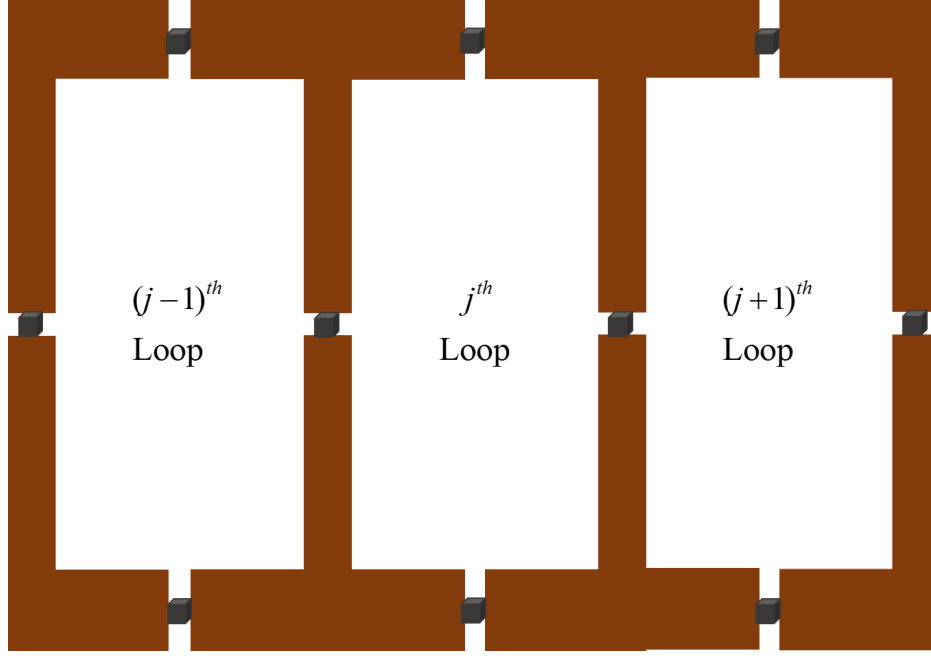


Figure 2.15: Planer view of three adjacent loops of the array coil.

The decoupling between two loops can be interpreted as isolation between them. In other words, Kirchhoffs voltage equation inside the j^{th} loop is supposed to be independent of mesh currents of the other loops. This objective can be satisfied by making coefficient of I_{j-1} and I_{j+1} zero in Eq. 2.56. This condition for I_{j-1} and I_{j+1} is respectively shown in Eq. 2.57 and Eq. 2.58.

$$\begin{aligned}
 & j\omega \left[2 \left(L_{j,j-1} - L'_{j,j-1} - \tilde{L}_{j,j-1} + \tilde{L}'_{j,j-1} \right) + \frac{1}{\omega^2 C_j^d} \right. \\
 & \quad + M_{j,j-1} - M'_{j,j-1} - M_{j+1,j-1} + M'_{j+1,j-1} \\
 & \quad \left. - M_{j,j} + M'_{j,j} + M_{j+1,j} - M'_{j+1,j} \right] I_{j-1} = 0
 \end{aligned} \tag{2.57}$$

$$\begin{aligned}
 & j\omega \left[2 \left(L_{j,j+1} - L'_{j,j+1} - \tilde{L}_{j,j+1} + \tilde{L}'_{j,j+1} \right) + \frac{1}{\omega^2 C_j^d} \right. \\
 & \quad + M_{j,j+1} - M'_{j,j+1} - M_{j+1,j+1} + M'_{j+1,j+1} \\
 & \quad \left. - M_{j,j+2} + M'_{j,j+2} + M_{j+1,j+2} - M'_{j+1,j+2} \right] I_{j+1} = 0
 \end{aligned} \tag{2.58}$$

Considering the shielding effects in Eq. 2.9 and rewriting the expression for $(j, j-1)^{th}$ element of the inductance matrix $\bar{\bar{K}}$ leads to the exactly same expression that is given as inductive terms in Eq. 2.57. In other words, Eq. 2.57 can be rearranged in the following form

$$K_{j,j-1} + \frac{1}{\omega^2 C_j^d} = 0 \tag{2.59}$$

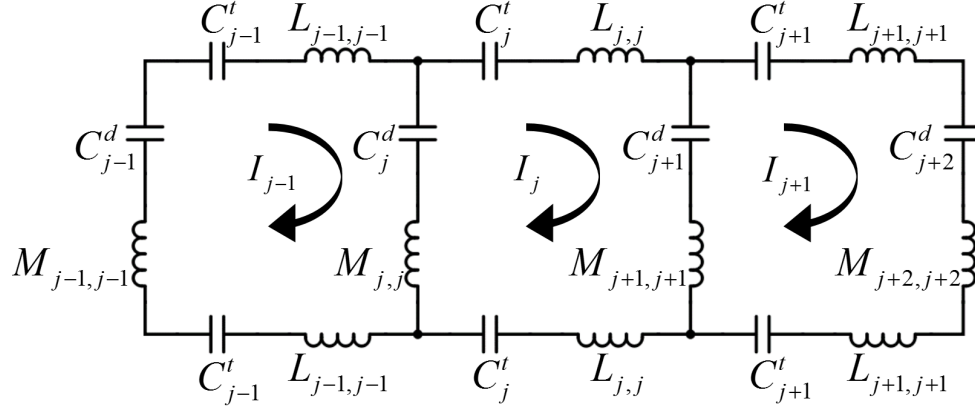


Figure 2.16: Equivalent circuit model of the three adjacent loops of the array coil.

Therefore, the proper value for decoupling capacitor can be obtained as follows

$$C_j^d = -\frac{1}{\omega^2 K_{j,j-1}} \quad (2.60)$$

Obviously, this capacitor value would decouple two adjacent loops perfectly, if and only if all connections are perfect electric conductor (PEC) and any other resistance effect does not exist. However, it is very optimistic to assume that such a perfect situation can be occurred in real life where the most significant resistance effect in MRI applications comes from imaging sample.

Tuning to the Desirable Resonant Frequency

Generally, in design of an array, decoupling procedures take first place of whole process. Assume that perfect decoupling between all channels is achieved then whole array structure can be treated as N separated single loop coils. This assumption makes the tuning procedure very easy and feasible. An isolated single loop inside the shield of RF-coil is shown in Fig. 2.17a.

Similar to the configuration discussed in the decoupling case, the equivalent circuit model of this case is achievable as shown in Fig. 2.17b.

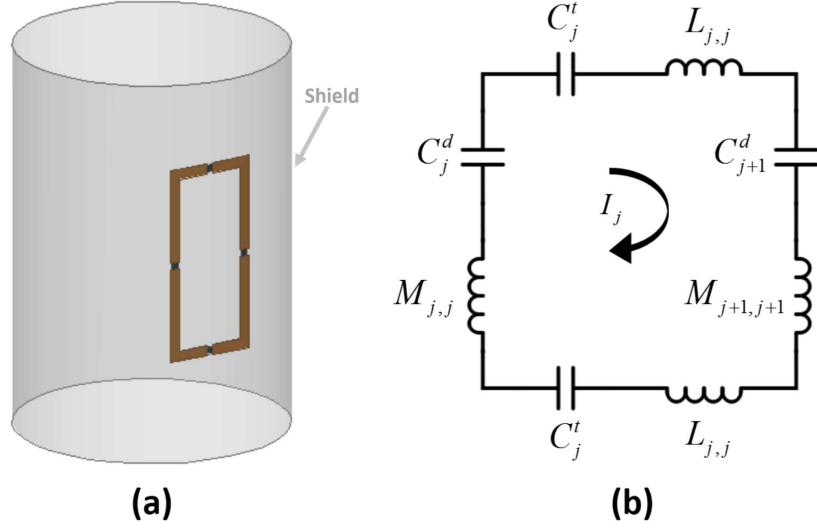


Figure 2.17: Single copper loop inside the RF shield. (a) Modal demonstration, (b) Equivalent circuit model.

Kirchhoff's voltage law for this single loop can simply be written as

$$\begin{aligned}
 j\omega \left[2 \left(L_{j,j} - L'_{j,j} - \tilde{L}_{j,j} + \tilde{L}'_{j,j} \right) + M_{j,j} - M'_{j,j} - M_{j+1,j} + M'_{j+1,j} \right. \\
 \left. - M_{j,j+1} + M'_{j,j+1} + M_{j+1,j+1} - M'_{j+1,j+1} - \frac{1}{\omega^2} \left(\frac{2}{C_j^t} + \frac{1}{C_j^d} + \frac{1}{C_{j+1}^d} \right) \right] I_j = 0
 \end{aligned} \tag{2.61}$$

Recalling the expression of $\{j, j\}^{th}$ element of the inductance matrix $\bar{\bar{K}}$ defined in Eq. 2.9 and comparing with the inductive terms of Eq. 2.61 eventuate that Eq. 2.61 can be written in the following form as well

$$j\omega \left[K_{j,j} - \frac{1}{\omega^2} \left(\frac{2}{C_j^t} + \frac{1}{C_j^d} + \frac{1}{C_{j+1}^d} \right) \right] I_j = 0 \tag{2.62}$$

Substituting the values of C_j^d and C_{j+1}^d from Eq. 2.60 into Eq. 2.62 and solving the equation for C_j^t determines the tuning capacitor value for j^{th} loop of the array as follows

$$C_j^t = \frac{2}{\omega^2} \left(\frac{1}{K_{j,j} + K_{j,j-1} + K_{j+1,j}} \right) \tag{2.63}$$

The capacitor values obtained for decoupling and tuning may cause a resonance in the desirable frequency, however, there is still a big issue in terms of power efficiency which is tightly related to the impedance matching between the coil and the transmission line (TL) used for power transmission.

Impedance Matching

Typically, 50Ω transmission lines (TL) are being used for power transmission purposes. Therefore, the impedance seen at the input port of the coil must be matched to 50Ω in order to achieve maximum power transmission from the source to the coil. Since in design of an RF-coil it is intensively avoided to use extra elements, especially inductive components, the matching is favorable to be achieved utilizing only the capacitors on end-rings and rungs. In terms of impedance matching, it is neither sufficient nor reasonable to take no-resistance assumption. Since the most significant purpose of this design is to transmit the power to the imaging sample, it must be somehow modeled in the equivalent circuit model. Fig. 2.18 presents an equivalent circuit model for three adjacent loops including body's loading effects as some distributed resistors on each loop.

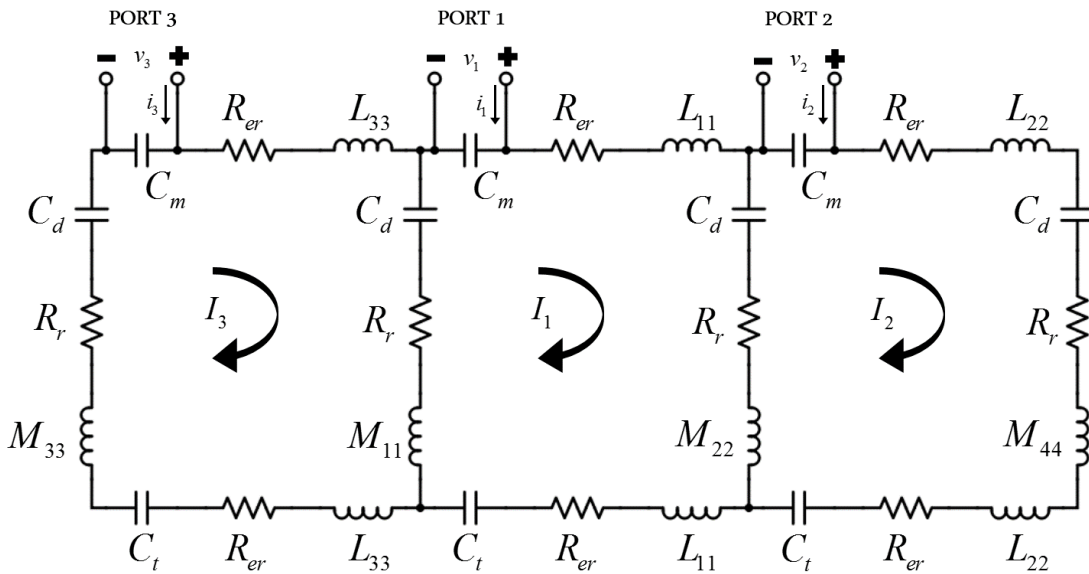


Figure 2.18: Equivalent circuit model of three adjacent loops of the array coil considering the load effect.

In the Fig 2.18, R_{er} and R_r denote the resistive effect of imaging sample on end-rings and rungs, respectively. Calculation of values of R_{er} and R_r is a very complicated procedure based on obtaining the scattering fields from the object

inside the coil. However, one can achieve a good prediction on these values by performing some EM simulations.

In the case shown in Fig. 2.18, two loops adjacent to the middle coil has been considered in the equivalent model and it is not reasonable anymore to deal with a single isolated loop like what we did in Fig. 2.17b. The reason makes Fig. 2.17.b invalid for the real case is that the real part of mutual impedance between two adjacent loops is not zero anymore and consequently perfectly decoupling are not possible using only one capacitive components, between two loops (still perfect decoupling of nonadjacent loops are assumed). Although the perfect isolation of adjacent loops is not possible, some techniques can be utilized to have maximum isolation as possible.

Most commonly used parameters as criteria for matching and decoupling are S-parameters such that lower S_{nn} and S_{mn} represent better matching and decoupling, respectively. Scattering matrix of a 3-port network with impedance matrix of $\bar{\bar{Z}}$ can be determined as follows [37]

$$\bar{\bar{S}} = (\bar{\bar{Z}} + \bar{\bar{Z}}_0)^{-1} \cdot (\bar{\bar{Z}} - \bar{\bar{Z}}_0) \quad (2.64)$$

Where matrix $\bar{\bar{Z}}_0$ denotes the characteristic impedance of transmission lines.

$$\bar{\bar{Z}}_0 = \begin{bmatrix} Z_0 & 0 & 0 \\ 0 & Z_0 & 0 \\ 0 & 0 & Z_0 \end{bmatrix} \quad (2.65)$$

Elements of the impedance matrix $\bar{\bar{Z}}$ for the equivalent circuit shown in Fig. 2.18 can be determined as follows

$$Z_{11} = \left. \frac{v_1}{i_1} \right|_{i_2=i_3=0} = -\frac{j}{\omega C_m} (1 - P_{11}) \quad (2.66)$$

$$Z_{21} = \left. \frac{v_2}{i_1} \right|_{i_2=i_3=0} = \frac{j}{\omega C_m} P_{11} T_{21} \quad (2.67)$$

$$Z_{31} = \left. \frac{v_3}{i_1} \right|_{i_2=i_3=0} = \frac{j}{\omega C_m} P_{11} T_{31} \quad (2.68)$$

$$Z_{33} = Z_{22} = Z_{11} \quad \& \quad Z_{12} = Z_{21} \quad \& \quad Z_{13} = Z_{31} \quad (2.69)$$

$$T_{21} = \frac{I_2}{I_1} \Big|_{i_2=i_3=0} = -\frac{R_{21} + j(\omega K_{21} - H_{21}/\omega)}{R_{22} + j(\omega K_{22} - H_{22}/\omega)} \quad (2.70)$$

$$T_{31} = \frac{I_3}{I_1} \Big|_{i_2=i_3=0} = -\frac{R_{31} + j(\omega K_{31} - H_{31}/\omega)}{R_{32} + j(\omega K_{33} - H_{33}/\omega)} \quad (2.71)$$

$$P_{11} = \frac{I_1}{i_1} \Big|_{i_2=i_3=0} = -\frac{j}{\omega C_m} \{R_{11} + T_{21}R_{21} + T_{31}R_{31} + j\omega [K_{11} + T_{21}K_{21} + T_{31}K_{31} - \frac{1}{\omega^2} (H_{11} + T_{21}H_{21} + T_{31}H_{31})]\}^{-1} \quad (2.72)$$

In Eq. 2.70-2.72, K and H components denote the elements of inductance (\bar{K}) and capacitance (\bar{H}) matrices presented in Eq. 2.9 and Eq. 2.10, respectively. Resistance matrix R is defined as

$$\bar{R} = \begin{bmatrix} 2R_{er} + 2R_r & -R_r & -R_r \\ -R_r & 2R_{er} + 2R_r & 0 \\ -R_r & 0 & 2R_{er} + 2R_r \end{bmatrix} \quad (2.73)$$

Coupling between two ports can be investigated using the definition of mutual impedance (Z_{21}) given in Eq. 2.67 and Eq. 2.68 such that if two ports are perfectly decoupled, excitation on the 1st port using current i_1 does not affect the 2nd port at all. In other words, it does not induce any voltage on the 2nd port and it means Z_{21} must be zero; however, in the real life case, perfect decoupling is not achievable which is clearly visible from equation Eq. 2.67 so that one cannot make Z_{21} zero. Similarly perfect matching occurs if the input impedance Z_{11} be equal to 50Ω (in typical TL case). Nevertheless, the equation $Z_{11} = 50$ for C_m may not have any solution.

Consequently, in order to achieve an acceptable design, an optimization algorithm on parameters of matching and decoupling should be performed.

Optimization of Tuning and Decoupling Parameters

Since S-parameters offer quantitative criteria for both matching and decoupling, a cost function can be defined as mismatch between recent S-parameters and desirable ones. This cost function should be minimized to achieve the desirable design. In section 2.2, the steepest descent method is explained in details as a

minimization approach. For this design problem, residual error can be defined as

$$\bar{e}(\bar{x}) = \begin{bmatrix} S_{11}(\bar{x}) - S_{11}^{goal} \\ S_{21}(\bar{x}) - S_{21}^{goal} \end{bmatrix} \quad (2.74)$$

Where model vector \bar{x} is

$$\bar{x} = \begin{bmatrix} C_t \\ C_d \\ C_m \end{bmatrix} \quad (2.75)$$

Eventually, the cost function is defined as

$$C(\bar{x}) = |\bar{e}(\bar{x})|^2 = |S_{11}(\bar{x}) - S_{11}^{goal}|^2 + |S_{21}(\bar{x}) - S_{21}^{goal}|^2 \quad (2.76)$$

According to the algorithm shown in Fig. 2.14, an initial prediction for model vector \bar{x} is needed. The value given in Eq. 2.63 may be a reasonable start point for both tuning and matching capacitors. Similarly C_d can be taken as its value in Eq. 2.60. The rest of the procedure is the same as expressed in section 2.2. This iterative method seeks for the desirable solution in the direction that cost function approaches to its minimum. The iterations will be stopped if the pre-defined condition is satisfied. The condition would be a sufficient minimum value for the cost function. Finally, at the end of the iterative process, appropriate values for tuning, decoupling, and matching capacitors will be available. Due to the symmetry of the structure, determined capacitor values can be used for all loops in the array.

2.3.2 Excitation of the Array

After achieving an appropriate design for the array, it needs to be excited in a correct manner so that be able to produce the desirable magnetic field.

Explicit Solution Using Equivalent Circuit Model

As discussed earlier, RF-coil of MR system is supposed to produce a homogeneous magnetic field inside the imaging region. Accordingly, proper excitation for the

birdcage coil is defined as quadrature excitation and current distribution on the whole birdcage structure corresponding to the quadrature excitation is expressed in details. Since the array designed in this thesis is a birdcage-like structure, the same current distribution with birdcage produces the same magnetic field profile which is a homogeneous field. In order to achieve the mentioned current distribution, the array should be excited with proper voltage values at the ports.

This array can be modeled as an N -port network shown in Fig. 2.19a.

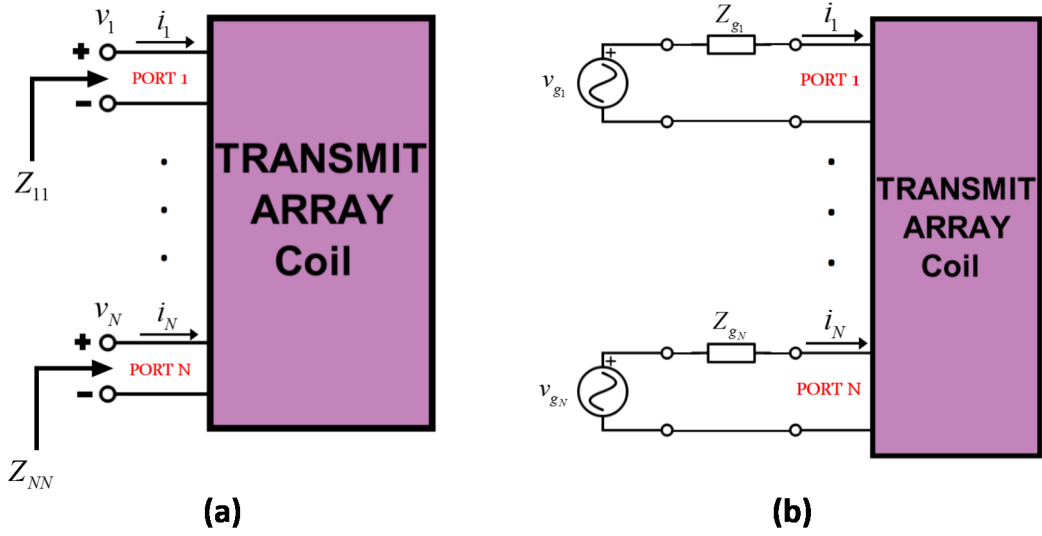


Figure 2.19: Block diagram model of an N -port network (a) with N -excitation (b).

Utilizing Eq. 2.66-2.72 and assuming perfect isolation (decoupling) between non-adjacent ports, elements of impedance matrix corresponding to the network in Fig. 2.19a can be determined as follows.

$$Z_{yx} = \left. \frac{v_y}{i_x} \right|_{\substack{i_z=0 \\ z \neq x}} = \begin{cases} -\frac{j}{\omega C_m} (1 - P_{xx}) & y = x \\ \frac{j}{\omega C_m} P_{xx} T_{yx} & |y - x| = 1 \\ 0 & |y - x| \geq 2 \end{cases} \quad (2.77)$$

$$T_{yx} = \left. \frac{I_y}{I_x} \right|_{\substack{i_z=0 \\ z \neq x}} = \begin{cases} 1 & y = x \\ -\frac{R_{yx} + j(\omega K_{yx} - H_{yx}/\omega)}{R_{yy} + j(\omega K_{yy} - H_{yy}/\omega)} & |y - x| = 1 \\ 0 & |y - x| \geq 2 \end{cases} \quad (2.78)$$

$$P_{yx} = \left. \frac{I_y}{i_x} \right|_{\substack{i_z=0 \\ z \neq x}} = \begin{cases} -\frac{j}{\omega C_m} \{R_{xx} + T_{x+1,x}R_{x+1,x} + T_{x-1,x}R_{x-1,x} \\ + j\omega [K_{xx} + T_{x+1,x}K_{x+1,x} + T_{x-1,x}K_{x-1,x} \\ - \frac{1}{\omega^2} (H_{xx} + T_{x+1,x}H_{x+1,x} + T_{x-1,x}H_{x-1,x})] \}^{-1} & y = x \\ t_{xx}T_{yx} & |y - x| = 1 \\ 0 & |y - x| \geq 2 \end{cases} \quad (2.79)$$

$$R_{yx} = \begin{cases} 2R_{er} + 2R_d & y = x \\ -R_d & |y - x| = 1 \\ 0 & |y - x| \geq 2 \end{cases} \quad (2.80)$$

Following matrix equation describes the N -port network shown in figure Fig. 2.19b in terms of voltages and currents at the ports

$$\bar{v} = \bar{Z} \cdot \bar{i} \quad (2.81)$$

Where vector \bar{v} consists of voltage values at the input of each port, \bar{i} includes corresponding port current, and \bar{Z} matrix is the impedance matrix. Furthermore, t_{yx} in Eq. 2.79 is defined as transfer coefficient from current at the x^{th} port, i_x , to the mesh current inside the y^{th} loop of the array, I_y , when all other ports are open. Therefore, the following matrix equation can be written as a relation between ports currents \bar{i} and corresponding loop currents \bar{I}

$$\bar{I} = \bar{P} \cdot \bar{i} \rightarrow \bar{i} = (\bar{P})^{-1} \cdot \bar{I} \quad (2.82)$$

Substituting Eq. 2.82 into Eq. 2.81 gives

$$\bar{v} = \bar{Z} \cdot (\bar{P})^{-1} \cdot \bar{I} \quad (2.83)$$

Connecting all ports to voltage generators with impedance of Z_g and writing mesh equations gives

$$\bar{v}_g = \bar{Z}_g \cdot \bar{i} + \bar{v} \quad (2.84)$$

Where \bar{Z}_g is generator impedance matrix and defined as

$$Z_{g,xy} = \begin{cases} Z_g & y = x \\ 0 & y \neq x \end{cases} \quad (2.85)$$

Substituting Eq. 2.82 and Eq. 2.83 into 4.31 leads to

$$\bar{v}_g = (\bar{\bar{Z}} + \bar{\bar{Z}}_g) \cdot (\bar{\bar{P}})^{-1} \cdot \bar{I} \quad (2.86)$$

In order to produce a homogeneous magnetic field inside the birdcage-like transmit array coil, the proper current distribution in the loops of the coil is given in section 2.1.1. Utilizing these current distribution as the well-known current vector \bar{I} in Eq. 2.86 leads to obtain the required voltage value at the each port so that the desirable magnetic field can be produced inside the coil.

Optimized Excitation

As discussed at motivations, one of the advantage of transmit array coil is providing a good controllability on profile of magnetic field and electric field. This can be applicable for homogeneity enhancement, local RF-shimming, and SAR reduction.

Since this array coil is a linear system, superposition theorem is valid and can be applied to the inputs and outputs of all channel. In other words, if voltage value at n^{th} port be assumed as n^{th} input and the magnetic or electric field inside the sample due to this voltage-excitation denote the corresponding n^{th} output, following equations express the total magnetic or electric field inside the sample due to N -port excitation

$$if \quad \bar{B}(V_n) = \bar{B}_n \Rightarrow \bar{B}(a_1V_1, \dots, a_NV_N) = \sum_{n=1}^N a_n \bar{B}_n \quad (2.87)$$

$$if \quad \bar{E}(V_n) = \bar{E}_n \Rightarrow \bar{E}(a_1V_1, \dots, a_NV_N) = \sum_{n=1}^N a_n \bar{E}_n \quad (2.88)$$

Where V_n denotes the voltage value at n^{th} port, \bar{B}_n and \bar{E}_n are magnetic and electric fields inside the coil due to V_n , and a_n is any arbitrary complex coefficient. Obviously, in order to apply the superposition theorem in such a way that offered above, the output due to the input on each channel must be known separately. These data can be extracted using some EM simulations or MR experiments. Once the output due to each channel obtained separately, this can be used in

optimization of field profiles inside the coil such that if any designated profile is desired, it can be achieved by employing a specific excitation.

Apparently, the steepest-descent method discussed in section 2.2 is suitable for this application. The target electric or magnetic field profile can be chosen as the goal solution and the cost function $C(\bar{x})$ will be defined as mismatch between target profile and the profile at each iteration. Furthermore, residual error vector $\bar{e}(\bar{x})$ consists of the difference between value of the field at each pixel and the target one. The model vector \bar{x} includes amplitudes and phases of voltages on the ports.

At the end of the iterative minimization presented in section 2.2, the proper voltage-excitations values will be available to produce the desirable magnetic or electric field.

Chapter 3

Experiments and Results

3.1 Coil Construction

The birdcage-like transmit array coil, designed and constructed in this thesis, is a head coil with diameter of 30cm and length of 30cm. As shown in Fig. 3.1, this array coil consists of 8 channels and each channel excites a rectangular loop of copper strips which are 1.5cm width.

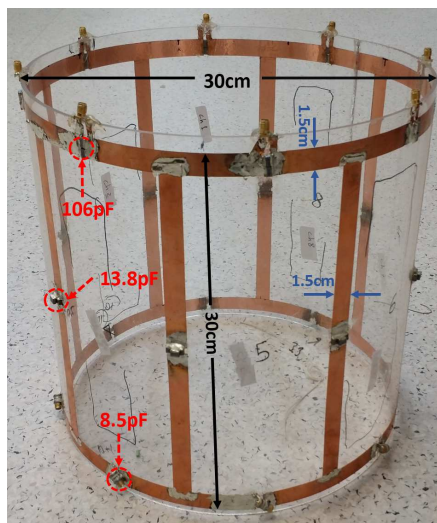


Figure 3.1: Constructed 8-channel birdcage-like Tx-array coil.

The capacitors, used on the upper end-ring, are for the matching purpose (C_m) and the value of these capacitors is $110pF$. The variable capacitors on the lower end-ring are introduced as tuning capacitors (C_t) in chapter 2. The value of these capacitors is calculated to be $8.5pF$, however, variable capacitors are utilized for fine tuning. Finally, in order for decoupling purpose a $13.8pF$ capacitor is used on the rungs of the coil (C_d).

Indeed, the capacitor values established in the coil construction are determined utilizing the method presented in chapter 2. Furthermore, a FEM-based simulation has been done before the constructions procedure in order to validate the analytical calculations.

Fig. 3.2 shows the structure that is been simulated using ANSYS HFSS v15.

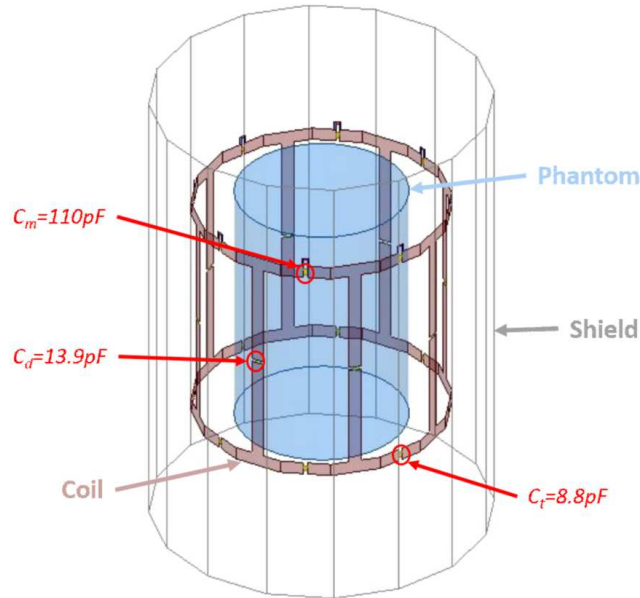


Figure 3.2: Simulated Tx-array Structure using ANSYS HFSS v15.

The calculated values for three kinds of capacitors in the Tx-array coil (C_t , C_m , and C_d) have error of less than 4% that is shown in Table 3.1.

Using the same method presented in chapter 2, an 8-rung band-pass birdcage coil has been constructed in order to compare the results of the array with. All dimensions of the birdcage is same with the array coil. However, the capacitor

Capacitors	Simulation	Experiment	Error
C_t	$8.8pF$	$8.5pF$	3.53%
C_m	$110pF$	$106pF$	3.77%
C_d	$13.9pF$	$13.8pF$	0.72%

Table 3.1: Capacitor values on the array coil, used in simulation and experiment.

values used in birdcage construction is totally different with array ones such that a $51pF$ capacitor is established on rungs, $21pF$ capacitors on upper and lower end-rings for tuning, and $26pF$ series capacitors at the ports in order for matching purpose. Constructed birdcage coil is shown in Fig. 3.3.

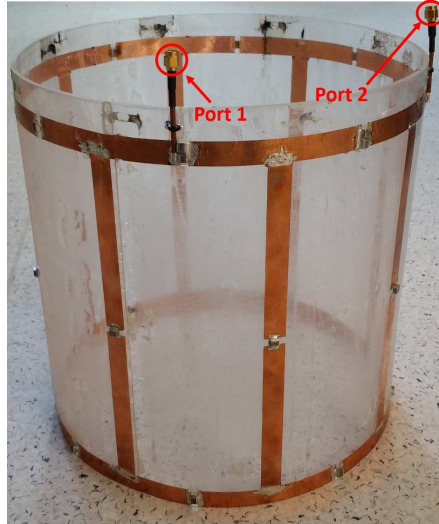


Figure 3.3: Constructed two-port head birdcage coil to compare with Tx-array coil.

3.2 Shield Construction

Construction of the RF-shield inside an MRI system always has been an important issue due to interaction between the shield and various components of the MR system such as the gradient coil. The gradient coil induces some amount of electric current on the RF-shield that is called eddy current. Locating this time varying current inside a magnet with a very strong magnetic field (B_0) causes an unwanted

force on the shield. This causes the shield to vibrate so this mechanical vibration may result in acoustic noise and image artifacts. Therefore, the shield should be designed in such a manner that prevents all RF-waves leaking out and/or squeezing in; on the other hand, the gradient field should be able to pass through the shield without any changes in the amplitude and/or phase, however, it should not induce eddy currents on the shield. According to [38, 39], slitting the shield with parallel slots along the z-direction meets the purpose of eliminating the eddy currents. However, these slots may cause some changes in RF-coil performance since RF-currents are flowing on the shield as well. Therefore, any changes on the shield will change the RF-current path and, consequently, RF-field. In order to avoid this effect some capacitors are placed between slots and they act like short circuits at high frequency (RF) but open circuits at low frequencies (gradient coil). The value of these capacitors in our design is $1nF$ which has impedance of 1.3Ω at $123MHz$ (RF) and $16K\Omega$ at $10KHz$ (gradient). Fig. 3.4 demonstrate the constructed shield including the mentioned slots and capacitors.

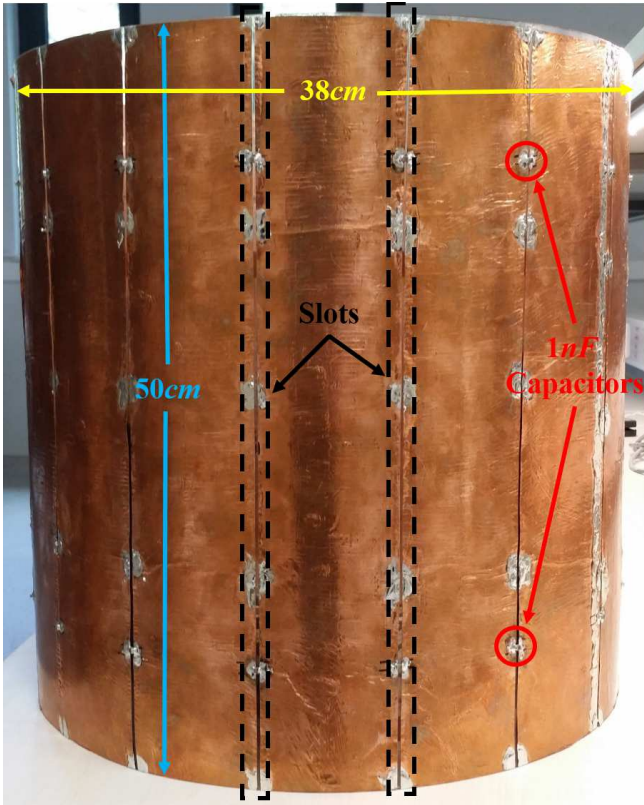


Figure 3.4: Constructed RF shield used in MR-experiment.

3.3 Experimental Setup

Since the constructed Tx-array coil has been used in transceiver mode, a home-made 8-channel T/R-switch made by Taner Demir of UMRAM, is utilized at input ports of the coil. This switch, shown in Fig. 3.5, provides a $27dB$ isolation between Tx and Rx modes.

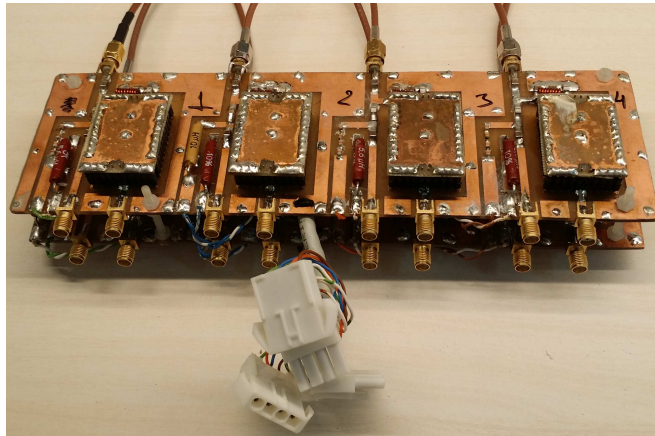


Figure 3.5: 8-channel T/R-switched used in MR-experiment in order to make using the the array coil as transceiver coil possible.

All images are acquired using the 8-channel Tx-array coil inside a 3T-Tim Trio MR scanner (Siemens Erlangen, Germany).

The phantom utilized for imaging is a cylindrical-shaped Nickel Chloride Hexahydrate solution, shown in Fig. 3.6.

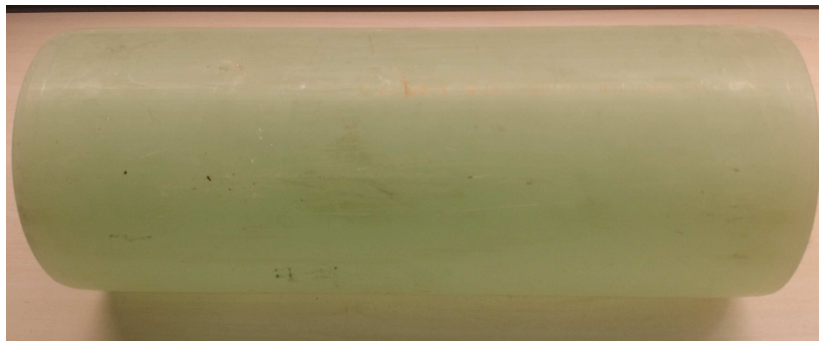


Figure 3.6: Nickel Chloride Hexahydrate solution used as a phantom for imaging.

3.4 Resonant Modes

Figure 3.7a shows input reflection coefficient in dB for the designed birdcage coil that achieved using simulation with ANSYS HFSS v15. Also, Fig. 3.7 is achieved by measuring S-parameters of the constructed birdcage coil using a network analyzer (Agilent, Baltimore, MD, United States).

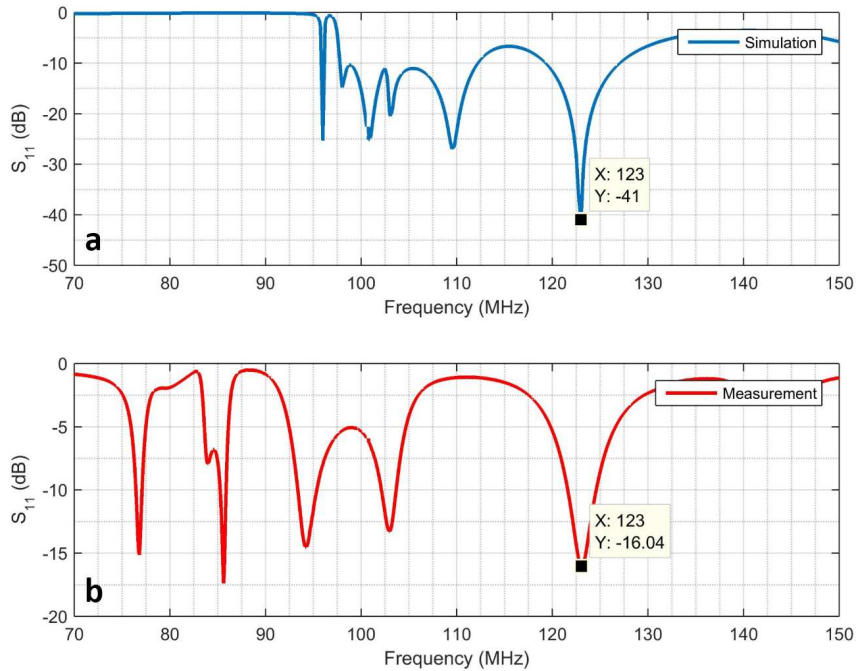


Figure 3.7: Demonstration of tuning and matching for the birdcage coil in simulation (a) and measurement (b).

Comparing Fig. 3.7a and Fig. 3.7b, the first mode of the birdcage coil, which is used in MRI, is the same in both simulation and experiment. The difference in magnitude of S_{11} is due to the PEC model of the coil used in simulation however, in the real-life structure they are lossy conductors (Copper). Although, the experimental structure is well-matched ($-16dB$) to 50Ω , as well.

Fig. 3.8a and Fig. 3.8b show input reflection coefficient in dB for the array in simulation and experiment, respectively. These figures indicate that the array

is well tuned at 123.2MHz (corresponding to our 3T MR scanner). Also, it is matched to 50Ω at 123.2MHz and input return loss is 15dB in experiment.

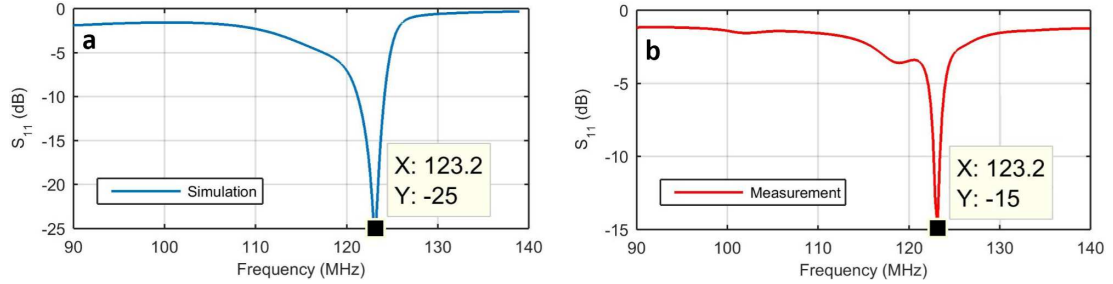


Figure 3.8: Demonstration of tuning and matching for the Tx-array coil in simulation (a) and measurement (b).

3.5 Coupling Between Channels

Measuring the S-parameters of the constructed array and plotting the S-parameters related to the coupling between the first channel and adjacent channels leads to, at least, 12dB decoupling between adjacent channels. This is shown in Fig. 3.9a and Fig. 3.9b for S_{21} and S_{81} , respectively.

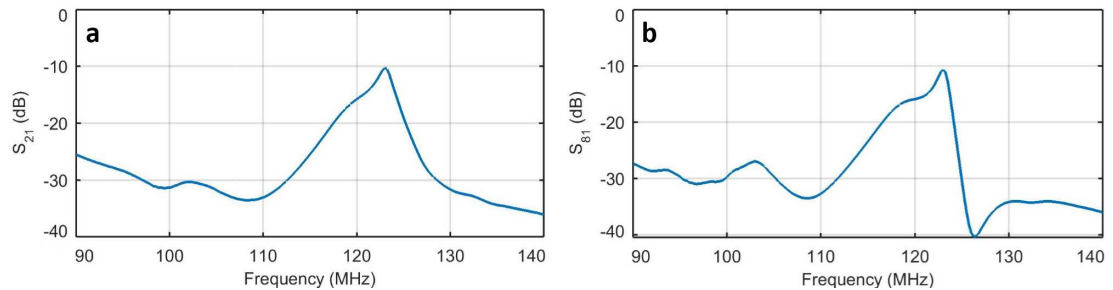


Figure 3.9: Demonstration of coupling between channel no.1 and adjacent channels in the Tx-array. (a) Channel 2, (b) Channel 8.

Fig. 3.10 shows the S-parameters related to the first channel of the Tx-array coil. These results are achieved by measurement. According to Fig. 3.10, coupling between nonadjacent channels is negligible. This was one of the design assumptions

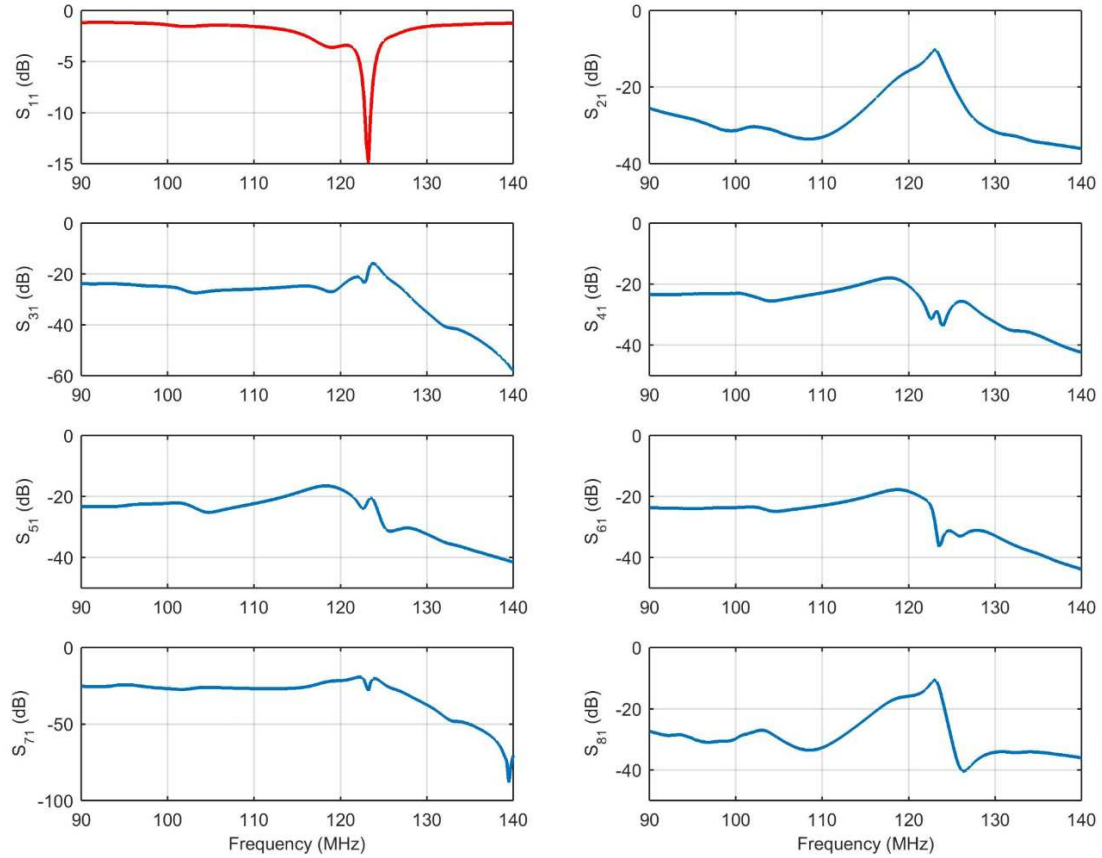


Figure 3.10: S-parameters, related to channel 1.

in chapter 2 that is confirmed in Fig. 3.10. This is also shown in Fig. 3.11 which is a graphical demonstration for S-matrix of the 8-ch Tx-array at 123.2MHz .

According to Fig. 3.11, the return loss at each port is 15dB , the decoupling between adjacent channels, in the worst case, is 12dB , and this is 19dB up to 32dB for nonadjacent channels.

Coupling phenomenon can be shown using B_1^+ -map, as well. Fig. 3.12 shows the B_1^+ -map inside the phantom for 8 cases. In each cases, only one channel is excited and all other seven channels are terminated with a 50Ω . B_1^+ -maps in Fig. 3.12a are simulation results and Fig. 3.12b is related to a MR experiment. All B_1^+ -maps in Fig. 3.12b are acquired using the Bloch-Siegert method [40, 41]. Since some magnetizations, in regions whose are not close enough to the exciting channel, experienced too small RF-excitation, they are not able to produce high-intensity

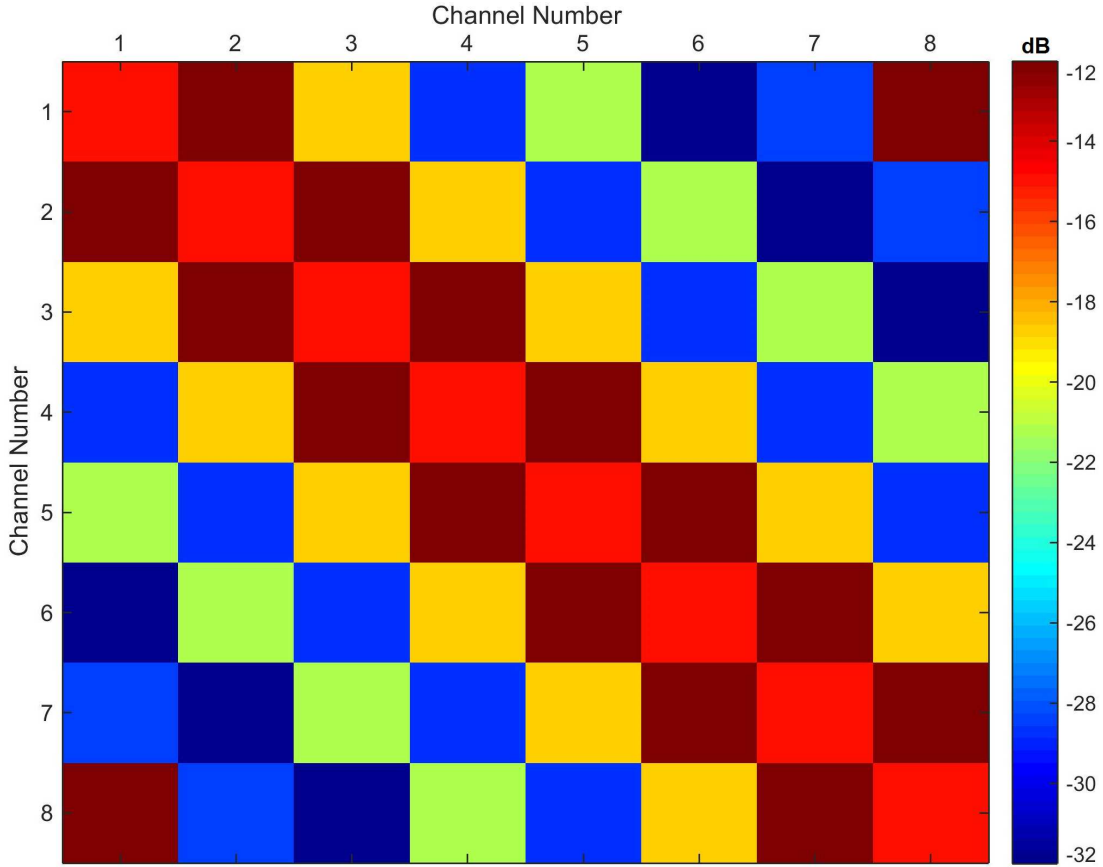


Figure 3.11: Graphical demonstration of S-matrix for the Tx-array.

RF-signal. Therefore, the coil measures a very small SNR for such regions so that the noise ruins the data corresponding to these regions (especially the phase of the data). Consequently, a proper mask is used in B_1^+ -map extraction technique in order to suppress the data acquired from such regions. This is the reason that some weird black holes are observable in Fig. 3.12b (Experiment data) while those are not showed up in Fig. 3.12a (simulation data) since the noise is not involved in simulation environment.

Fig. 3.13a is B_1^+ -maps when only an individual channel is excited and Fig. 3.13b is MR-images of the same situations. Image contrast of all B_1^+ -maps and MR-images in Fig. 3.13 are saturated for the purpose of comparison.

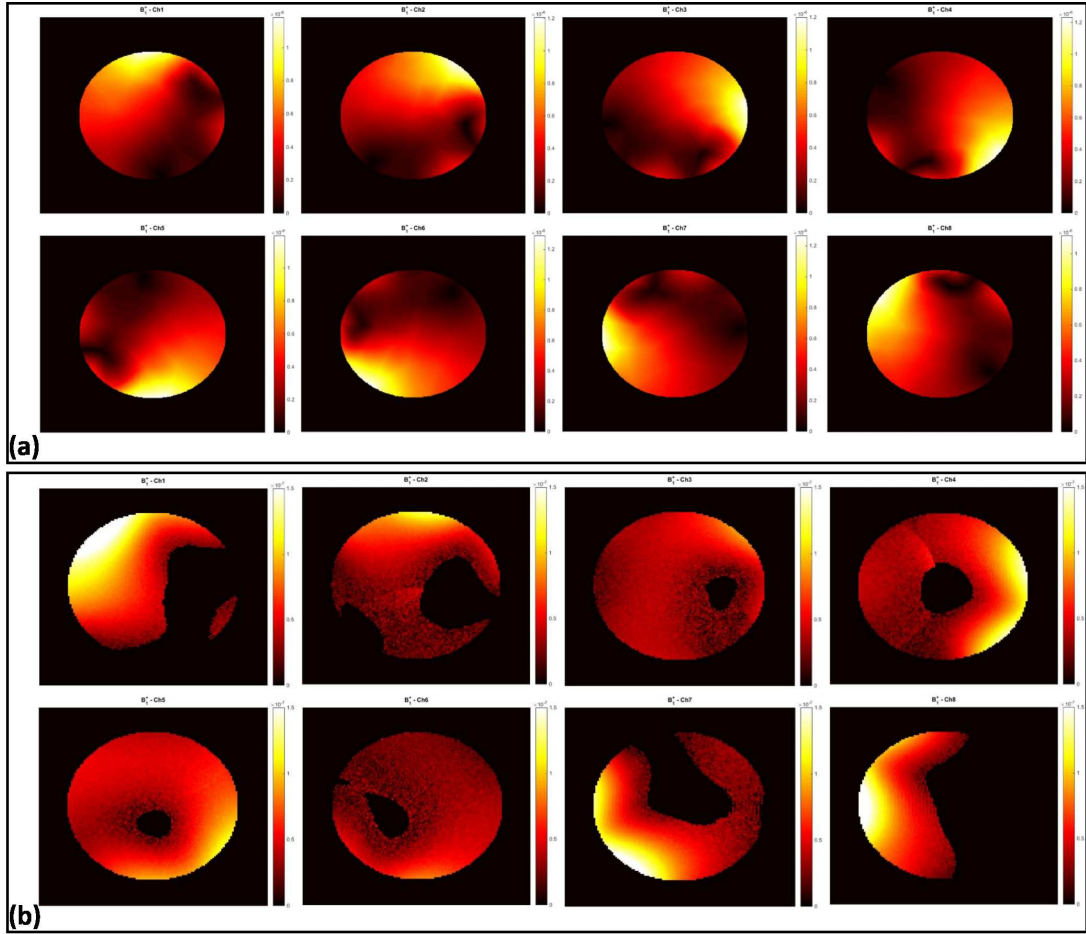


Figure 3.12: B_1^+ -map inside the phantom produced by each individual channel of the Tx-array coil in simulation (a) and MR-experiment (b). The features of the MR-experiment are: TR = 8.6s, TE = 6ms, NEX = 1, 128×128 , FOV = 20cm, and slice thickness = 5mm.

3.6 Homogeneity

According to Fig. 3.12, each channel has a specific B_1^+ profile, therefore applying the optimization technique explained in 2.3.2 leads to a homogeneous B_1^+ inside the phantom.

Fig. 3.14a shows the B_1^+ -map inside the phantom related to a well-designed band-pass birdcage coil which operates in circularly polarized (CP) mode. This result is achieved using a FEM-simulation. Fig. 3.14b shows the simulated B_1^+ -map

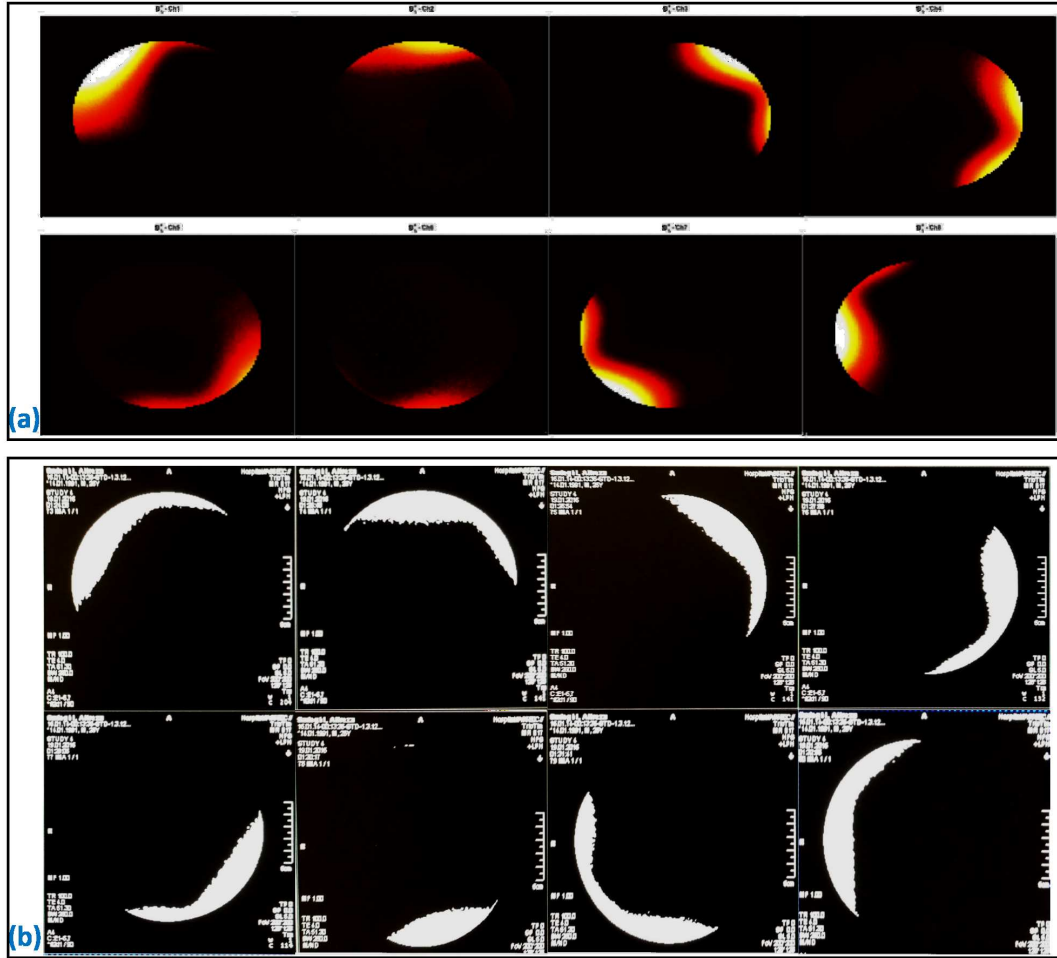


Figure 3.13: A demonstration for individual channels excitation in a MR-experiment, (a) B_1^+ -map, (b) MR-image. The MR-images in (b) are acquired using a gradient echo (GRE) pulse sequence (TR = 100s, TE = 4ms, NEX = 4, 128×128 , FOV = 20cm, and slice thickness = 5mm).

inside the phantom produced by the Tx-array coil that the voltage-excitations of the coil is achieved using the optimization. Fig. 3.14c is the corresponding B_1^+ -map extracted from a MR experiment and Fig. 3.14d is the MR-image of this experiment.

In this optimization, the constraints were to achieve as much homogeneous B_1^+ as possible and also to produce the minimum value of the electric field inside phantom. Since the birdcage coil is the structure that is being utilized in conventional MR scanners, B_1^+ -map of the Tx-array coil is compared to the B_1^+ -map of

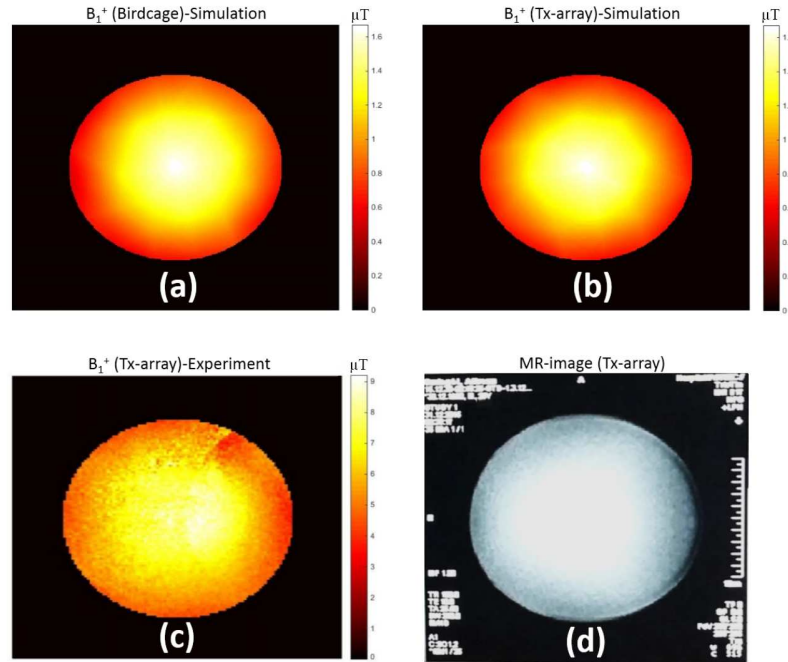


Figure 3.14: CP excitation inside the phantom and B_1^+ -maps corresponding to simulation of the birdcage coil (a), simulation of the Tx-array (b), and MR-experiment of the Tx-array (c). Corresponding MR-image using the Tx-array (d). The MR-image is acquired using a GRE pulse sequence ($TR = 100\text{s}$, $TE = 10\text{ms}$, $NEX = 1$, 128×128 , $FOV = 20\text{cm}$, slice thickness = 5mm , and flip angle = 79.5°).

the birdcage coil. This operational mode guarantees the maximum intensity and homogeneity of B_1^+ and also minimum value of the electric field simultaneously, both at the center of the coil.

Fig. 3.15a shows the distribution of B_1^+ along the x- and y-axes for the birdcage coil. Also, Fig. 3.15b shows the same parameter for the Tx-array coil.

According to Fig. 3.15, the relative standard deviation on x-axis for the birdcage coil is 42% however this is 38% for the Tx-array coil and this indicates more homogeneity on x-axis for the Tx-array coil. Although, the relative standard deviation on y-axis for both of the coils is 39%.

This phenomenon is more visible in circular paths. Fig. 3.16a and Fig. 3.16b show the B_1^+ distribution on circles with radii of 1cm , 3cm , 5cm , 7cm , and 9cm for the

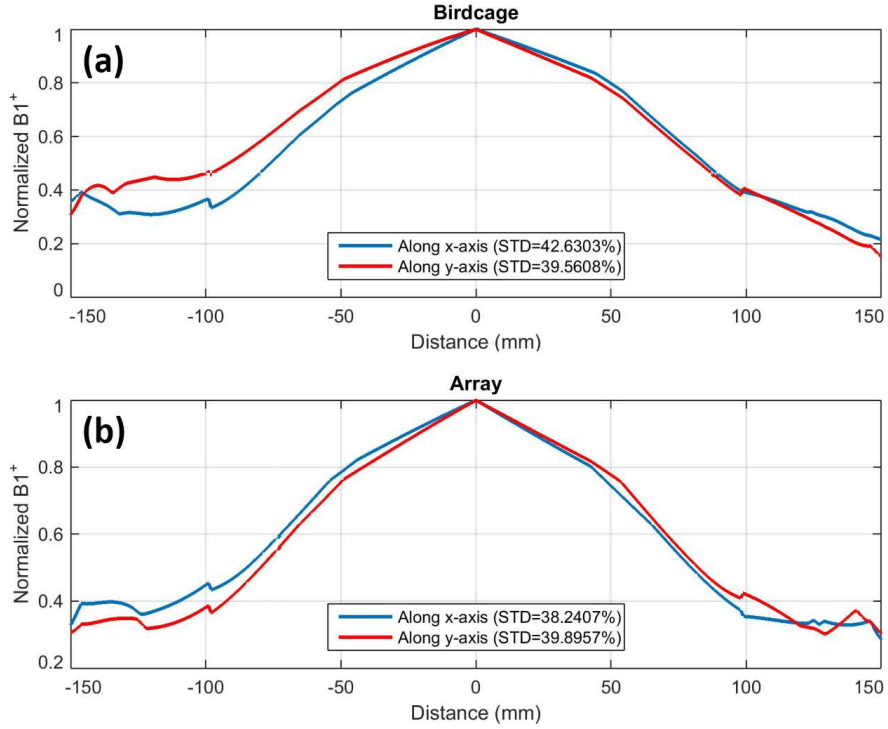


Figure 3.15: Distribution of B_1^+ on transversal axes for the birdcage coil (a) and Tx-array coil (b).

birdcage coil and Tx-array coil, respectively. Accordingly, Fig. 3.16c shows the relative standard deviation on corresponding circles for both of the coils.

According to Fig. 3.16c, the homogeneity of B_1^+ is descending outward the phantom and this phenomenon is occurring faster for the birdcage coil such that on the circle with radius of 9cm, the relative standard deviation is 10% for the birdcage coil however it is less than 5% for the Tx-array coil. Consequently, the performance of the birdcage coil in terms of B_1^+ homogeneity is achieved using Tx-array coil furthermore at some regions, even better performance is achieved.

However, in some MR-experiments, the homogeneity of the B_1^+ is more remarkable criterion than SAR level. Conventional birdcage coil is not capable to include the significance of these parameters while the Tx-array provides the opportunity to exclude the electric field from the constraints of the optimization. Fig. 3.17a and 3.17b demonstrate a comparison between B_1^+ homogeneity produced by the

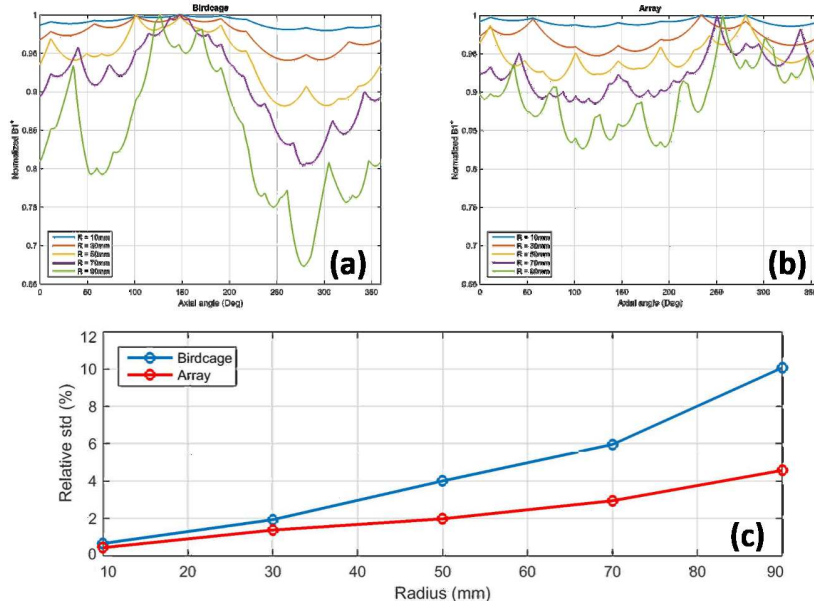


Figure 3.16: Distribution of normalized B_1^+ on transversal circles with radii of 1cm, 3cm, 5cm, 7cm, and 9cm for the birdcage coil (a) and Tx-array coil (b); and relative standard deviation of B_1^+ on transversal circles for both birdcage and Tx-array coil.

birdcage's operational mode and an optimized Tx-array without electric field constraint. As observed from Fig. 3.15a, relative standard deviation corresponding to the birdcage coil is 42% and 39% respectively on x- and y-axis. However, the corresponding value for the Tx-array coil, extracted from Fig. 3.17b, is 7.5% on both x- and y-axes. Nevertheless, since the minimum-electric-field constraint has been excluded from the optimization algorithm in order to increase the homogeneity of B_1^+ , the electric field has been crucially increased. Fig. 3.17c demonstrates the electric field profile, corresponding to the birdcage mode, while the profile in Fig. 3.17d is corresponding to the homogeneous excitation in Fig. 3.17b. Comparison between Fig. 3.17c and 3.17d shows that the electric field is increased up to three times at some regions which leads to significant increase in SAR level.

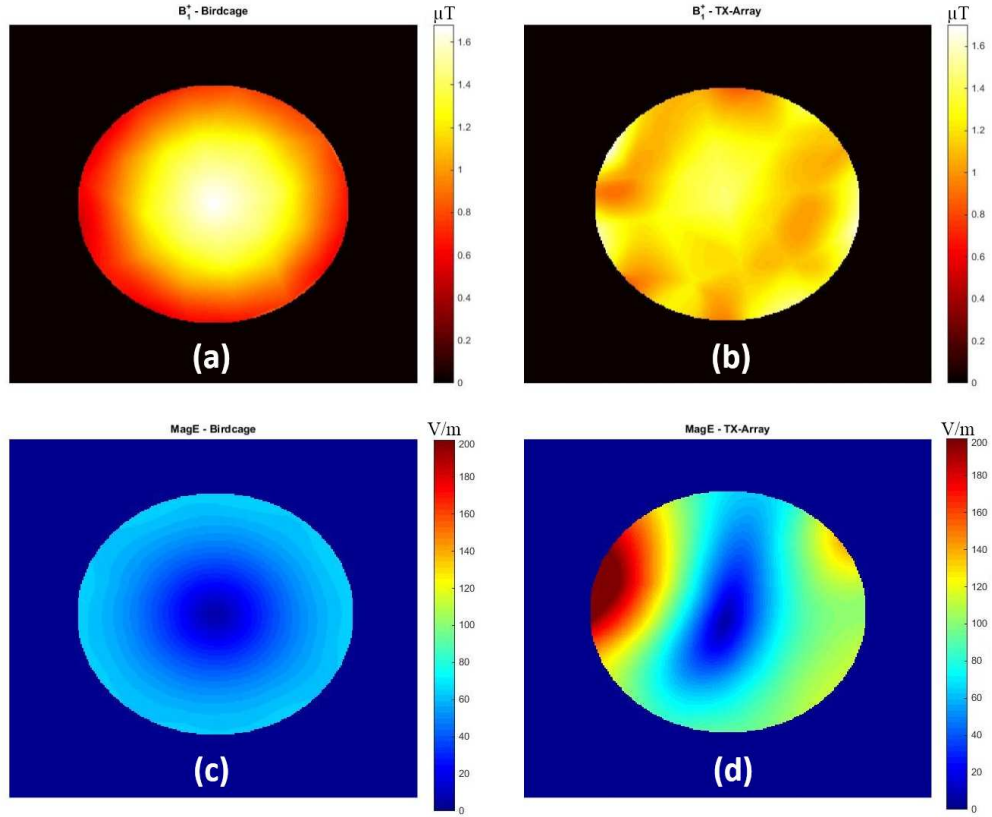


Figure 3.17: Demonstration of B_1^+ -map inside the phantom produced by (a) a quadrature-excited birdcage coil and (b) the Tx-array that is optimized without consideration of SAR. Electric field demonstration for the corresponding (c) birdcage, and (d) Tx-array coil.

3.7 Field Efficiency

In literature [42,43], B_1^+ efficiency at each position for a transmit RF coil is defined as ratio of the value of magnitude of the B_1^+ at that position to the square root of total input power. This ratio can be written as Eq. 3.1.

$$\eta(x, y, z) = \frac{|(B_1^+(x, y, z))|}{\sqrt{\text{Total input power}}} \quad (3.1)$$

Substituting the B_1^+ values, at the center of the phantom, obtained from Fig. 3.14a-c into Eq. 3.1 leads to the efficiency values of $1.7\mu T/\sqrt{W}$ for the birdcage coil, $1.7\mu T/\sqrt{W}$ for the Tx-array coil in simulation, and $1.65\mu T/\sqrt{W}$ for the Tx-array coil in the MR experiment. The efficiency values are given in

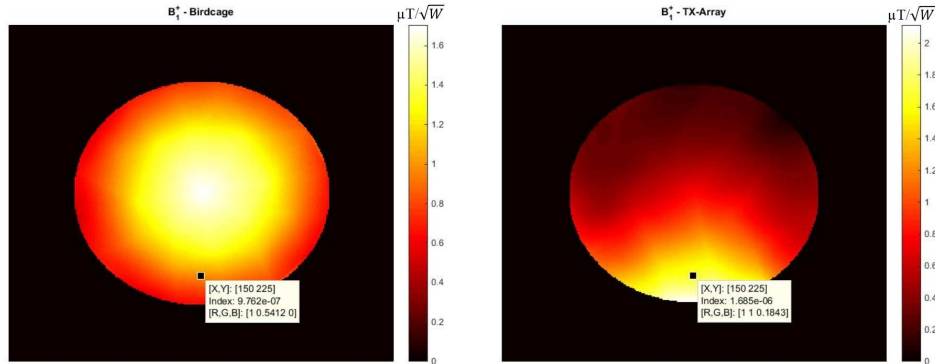


Figure 3.18: Demonstration of efficiency-map inside the phantom produced by (a) a quadrature-excited birdcage coil, and (b) the Tx-array that is optimized to achieve high efficiency at a region close to surface of the phantom.

Table 3.2. These values are strongly dependent on dimensions of the coils, material of the phantom, and etc which means the values are not restricted for any coil. Here, the values are presented to have better insight. Indeed, presenting in percentage form will be more appropriate. Simulation results for efficiency of the Tx-array is 100% matched to the efficiency of the birdcage coil at the center. Experimental results show that the efficiency of the Tx-array is only 3% less than the birdcage’s one.

Coil	Birdcage	Tx-array (Sim.)	Tx-array (Exp.)
Efficiency ($\mu T / \sqrt{W}$)	1.7	1.7	1.65

Table 3.2: B_1^+ efficiency comparison between the birdcage coil and the Tx-array. All values are related to the center of the phantom.

On the other hand, as discussed earlier, efficiency of the birdcage coil is remarkably high at the center of the coil although it is crucially low at the edges of the coil. This would be a critical disadvantage if one tries to image a region of interest close to the edge of the phantom. Choosing appropriate constraints makes the Tx-array capable to operate more efficient than a birdcage coil at the vicinity of the surface of the phantom. Fig. 3.18b is corresponding to the Tx-array coil that is acquired utilizing constraint of high efficiency at an arbitrary position close to surface of the phantom. Observable from Fig. 3.18, the efficiency of the birdcage

coil at that position is $0.98\mu T/\sqrt{W}$ while it is $1.69\mu T/\sqrt{W}$ for the Tx-array coil which is improved more than 72% with respect to the performance of the birdcage coil at that position.

3.8 Local B_1^+ Shimming

In order to show that the modes rather than birdcages CP mode are achievable using Tx-array coil, Fig. 3.19a is taken as a goal B_1^+ -map and after a proper optimization, B_1^+ -map shown in Fig. 3.19b is achieved in simulation.

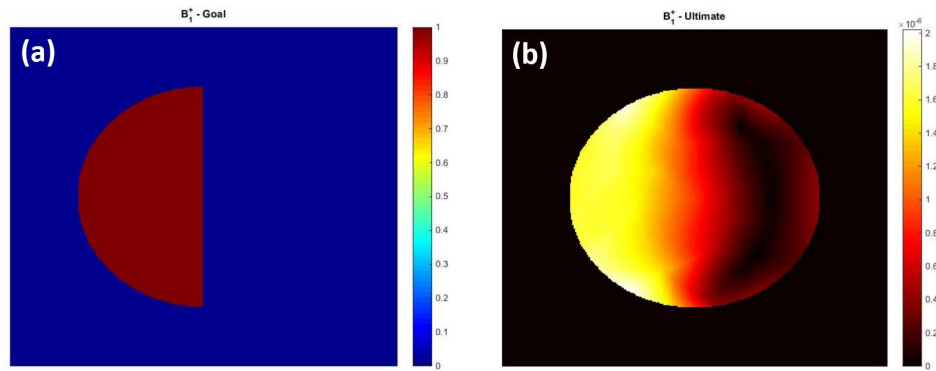


Figure 3.19: An arbitrary B_1^+ excited inside the phantom by the Tx-array coil. (a) The expected B_1^+ -map, (b) The achieved B_1^+ -map.

3.9 Local Electric-field-reduction

Since the strength of electric field is the most determinative parameter for SAR level, local reduction of the electric field may leads to the local SAR reduction. As shown in Fig. 3.20a, the electric field produced by CP mode of the birdcage coil is minimum at the center and it is ascending toward the surface of the phantom. However, for some applications, the minimum of the electric field is needed to be off-center as shown in Fig. 3.20b which is the goal of the optimization.

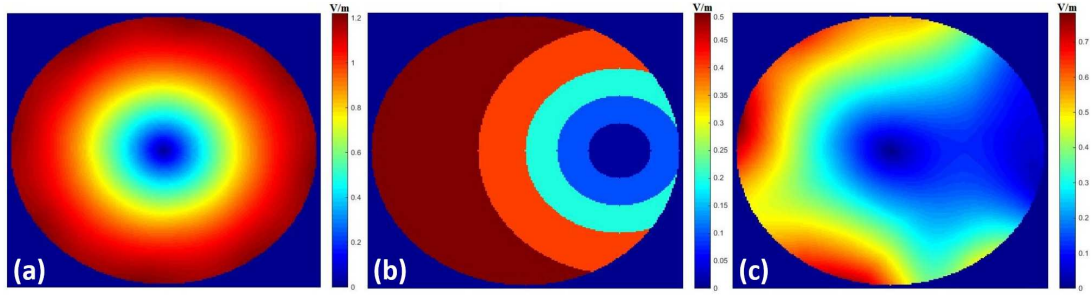


Figure 3.20: (a) The electric field distribution corresponding to CP excitation of a birdcage coil, (b) The goal electric field with off-center minimum, and (c) The optimized electric field corresponding to the Tx-array.

Consequently, the optimized electric field is achieved by simulation as Fig. 3.20c. This achievement is the direct resultant of the high-controllability of electric and magnetic field using Tx-array coils.

Chapter 4

Discussion

In this thesis, design of a birdcage-like Tx-array coil using an equivalent circuit model is studied. The presented circuit model contains many inductors which are representing the copper strips of the coil, however, this modeling is only valid if the wavelength is much greater than the size of the strips. In other words, in high frequencies where the wavelength is comparable to size of the coil, modeling the conductive strips with a single inductive element is not valid, instead, an N-stage RLC network should be utilized to model a single conductive strip [44]. Furthermore, at high frequencies (ultra high field MRI), exciting the Tx-array just like a birdcage coil does not produce a homogeneous magnetic field inside the coil at all [45]. On the other hand, the method established on this thesis for inductance calculations is still an approximation, so this method is not able to predict all self and mutual inductances without any error. Indeed, this is why we observe some error values in 3.1.

In addition, the capacitors used to built the coil are not perfectly-manufactured so that some amounts of tolerances are reported for these capacitors. These random tolerances are one of the most important issues makes the design procedure imperfect while the decoupling phenomenon is very sensitive to value of the decoupling capacitor.

FEM-based simulations play very significant roles in this design, however, there are some limitations in use of these simulations. For instance, if one tries to use material with finite conductivity as strips of the coil in simulation, the amount of required physical memory on the processing system (workstation) is almost unreachable due to the very tiny mesh sizes needed to be established inside the such a material, therefore, utilizing perfect electrical conductor (PEC) instead of copper might be a good solution. Obviously, this is not perfectly matched with the real-life case. This is the main reason of the mismatches occurred in Fig. 3.7 and 3.8 between simulation and measurement results.

The main claim of this thesis is to achieve the capability of controlling the electric and magnetic field inside the region of interest. This claim is obviously valid only if the field profiles corresponding to each channel is well-known, separately. Then superposing the profiles, using the amplitudes and phases obtained from the optimization, leads to the desirable B_1^+ -profile and minimized SAR. However, acquiring the field profiles inside the phantom correctly for each channel requires an acceptable signal-to-noise ratio (SNR) level at every points inside the phantom which seems not to be achievable for the points far away from the intended channel. Since a pretty good decoupling between channels is established, each loop of the Tx-array performs like a single surface coil so the SNR level decreases with factor of $1/\sqrt{r^5}$ [46] where r is the distance between the coil and intended position. Consequently, the B_1^+ -map corresponding to each channel is reliable only in some regions of the phantom close to that channel. In order to eliminate the unreliable data (low SNR), a mask is used in the B_1^+ -map extraction code. This is why some weird zero regions are observable in Fig. 3.12b. This may cause some errors in the results of the optimization which can be observed in Fig. 3.14c,d at the right side of the phantom where the homogeneity is a little bit ruined.

Eventually, as a future work, adjusting the electric field inside the human body can be performed. one of the critical issues of imaging a patient with an implant inside his/her body is increasing the temperature of the conductor of the implant due to the induced electric current on it. This effect can remarkably be decreased by minimizing the electric field locally at vicinity of the implant. Theory and

simulations of this method is on progress and Fig. 3.20 shows that the electric field is adjustable inside a phantom. Enforcing the electric field to be zero, inside the human body at vicinity of the implant, would solve the heating issue of implants during MRI.

Chapter 5

Conclusion

In this thesis, configuration of very well-known birdcage-like coil is used as an eight-channel RF transmit array coil. The design is based on the equivalent circuit model of the coil and the capacitive decoupling method is used in order to decouple the adjacent channels. The method presented in this study satisfies more than 12dB decoupling between adjacent channels and up to 32dB decoupling for nonadjacent channels. Also applying an optimization (the steepest-descent method) to the equivalent circuit model provides more than 15dB return loss for each input port.

Comparing this Tx-array coil to a birdcage coil with the same size, Tx-array coil provides a slightly better homogeneity when it is operating in CP mode of the birdcage. On transverse plane along x-axis of the coordinate system of the MR scanner, relative standard deviation of B_1^+ for the birdcage coil is 42%, however, this is 38% for the Tx-array coil. Although, this value on the y-axis for both of the coils is 39%. Indeed, advantage of the Tx-array coil from homogeneity point of view comes to the picture if B_1^+ values acquired circumferentially inside the object. Results show that the performance of both coils are the same at the central region of the coil however, it decreases crucially for the birdcage toward the edges of the object such that the relative standard deviation of B_1^+ at the boundary of the imaging phantom is 10% for the birdcage and it is 5% for the Tx-array coil.

Furthermore, for the applications that the SAR level is less-significant criterion, the homogeneity in radial direction could be remarkably enhanced utilizing the Tx-array coil such that the relative standard deviation on both x-and y-axes is 7.5%, however, it is about 40% for the birdcage coil.

Unlike the other designs for Tx-array coils, this design can also perform very similar to the birdcage coil even from the efficiency point of view. Results show $1.7\mu T/\sqrt{W}$ efficiency at the center of phantom for the birdcage coil and this is $1.65\mu T/\sqrt{W}$ for the birdcage-like Tx-array coil, however for the similar size of the head coil, Shajan et al. [18] achieved $0.85\mu T/\sqrt{W}$ using their own Tx-array coil. This means that our Tx-array coil achieved the efficiency at the center of the coil only 3% less than the birdcage's one however, the Tx-array coil of Shajan et al. achieved 50% less efficiency. In addition, the birdcage-like Tx-array coil performs much better than the birdcage coil at regions close to the surface of the phantom so that at such a region, we achieved more than 72% better efficiency versus the birdcage coil (Fig. 3.18).

Ultimately, desirable B_1^+ -profile and minimum electric field as constraints of the optimization is applied to voltage-excitations of the Tx-array and the result is shown as the proof-of-concept. Furthermore, the same optimization technique with constraint of the desirable position for zero-electric-field is performed which provides an opportunity for local electric-field-reduction.

Bibliography

- [1] C. E. Hayes, W. A. Edelstein, J. F. Schenck, O. M. Mueller, and M. Eash, “An efficient, highly homogeneous radiofrequency coil for whole-body nmr imaging at 1.5 t,” *Journal of Magnetic Resonance (1969)*, vol. 63, no. 3, pp. 622–628, 1985.
- [2] H. Homann, I. Graesslin, H. Eggers, K. Nehrke, P. Vernickel, U. Katscher, O. Dössel, and P. Börnert, “Local sar management by rf shimming: a simulation study with multiple human body models,” *Magnetic Resonance Materials in Physics, Biology and Medicine*, vol. 25, no. 3, pp. 193–204, 2012.
- [3] B. van den Bergen, C. A. van den Berg, D. W. Klomp, and J. J. Lagendijk, “Sar and power implications of different rf shimming strategies in the pelvis for 7t mri,” *Journal of Magnetic Resonance Imaging*, vol. 30, no. 1, pp. 194–202, 2009.
- [4] P. Vernickel, P. Röschmann, C. Findekle, K.-M. Lüdeke, C. Leussler, J. Overweg, U. Katscher, I. Graesslin, and K. Schuenemann, “Eight-channel transmit/receive body mri coil at 3t,” *Magnetic Resonance in Medicine*, vol. 58, no. 2, pp. 381–389, 2007.
- [5] W. Mao, M. B. Smith, and C. M. Collins, “Exploring the limits of rf shimming for high-field mri of the human head,” *Magnetic resonance in medicine*, vol. 56, no. 4, pp. 918–922, 2006.
- [6] C.-L. Chin, C. M. Collins, S. Li, B. J. Dardzinski, and M. B. Smith, “Bird-cagebuilder: Design of specified-geometry birdcage coils with desired current

- pattern and resonant frequency,” *Concepts in Magnetic Resonance*, vol. 15, no. 2, pp. 156–163, 2002.
- [7] V. Alagappan, J. Nistler, E. Adalsteinsson, K. Setsompop, U. Fontius, A. Zelinski, M. Vester, G. C. Wiggins, F. Hebrank, W. Renz, *et al.*, “Degenerate mode band-pass birdcage coil for accelerated parallel excitation,” *Magnetic resonance in medicine*, vol. 57, no. 6, pp. 1148–1158, 2007.
- [8] C. Thalhammer, W. Renz, L. Winter, F. Hezel, J. Rieger, H. Pfeiffer, A. Graessl, F. Seifert, W. Hoffmann, F. von Knobelsdorff-Brenkenhoff, *et al.*, “Two-dimensional sixteen channel transmit/receive coil array for cardiac mri at 7.0 t: Design, evaluation, and application,” *Journal of Magnetic Resonance Imaging*, vol. 36, no. 4, pp. 847–857, 2012.
- [9] A. Graessl, W. Renz, F. Hezel, M. A. Dieringer, L. Winter, C. Oezerdem, J. Rieger, P. Kellman, D. Santoro, T. D. Lindel, *et al.*, “Modular 32-channel transceiver coil array for cardiac mri at 7.0 t,” *Magnetic resonance in medicine*, vol. 72, no. 1, pp. 276–290, 2014.
- [10] A. Gräßl, L. Winter, C. Thalhammer, W. Renz, P. Kellman, C. Martin, F. von Knobelsdorff-Brenkenhoff, V. Tkachenko, J. Schulz-Menger, and T. Niendorf, “Design, evaluation and application of an eight channel transmit/receive coil array for cardiac mri at 7.0 t,” *European journal of radiology*, vol. 82, no. 5, pp. 752–759, 2013.
- [11] Y. Eryaman, B. Akin, and E. Atalar, “Reduction of implant rf heating through modification of transmit coil electric field,” *Magnetic resonance in medicine*, vol. 65, no. 5, pp. 1305–1313, 2011.
- [12] Y. Eryaman, E. A. Turk, C. Oto, O. Algin, and E. Atalar, “Reduction of the radiofrequency heating of metallic devices using a dual-drive birdcage coil,” *Magnetic resonance in medicine*, vol. 69, no. 3, pp. 845–852, 2013.
- [13] B. van den Bergen, C. A. Van den Berg, L. W. Bartels, and J. J. Lagendijk, “7 t body mri: B1 shimming with simultaneous sar reduction,” *Physics in medicine and biology*, vol. 52, no. 17, p. 5429, 2007.

- [14] Y. Zhu, “Parallel excitation with an array of transmit coils,” *Magnetic Resonance in Medicine*, vol. 51, no. 4, pp. 775–784, 2004.
- [15] I. R. Connell, K. M. Gilbert, M. A. Abou-Khousa, and R. S. Menon, “Mri rf array decoupling method with magnetic wall distributed filters,” *Medical Imaging, IEEE Transactions on*, vol. 34, no. 4, pp. 825–835, 2015.
- [16] J. Wang *et al.*, “A novel method to reduce the signal coupling of surface coils for mri,” in *Proceedings of the 4th Annual Meeting of ISMRM*, p. 1434, 1996.
- [17] G. Shajan, M. Kozlov, J. Hoffmann, R. Turner, K. Scheffler, and R. Pohmann, “A 16-channel dual-row transmit array in combination with a 31-element receive array for human brain imaging at 9.4 t,” *Magnetic resonance in medicine*, vol. 71, no. 2, pp. 870–879, 2014.
- [18] G. Shajan, C. Mirkes, K. Buckenmaier, J. Hoffmann, R. Pohmann, and K. Scheffler, “Three-layered radio frequency coil arrangement for sodium mri of the human brain at 9.4 tesla,” *Magnetic resonance in medicine*, vol. 75, no. 2, pp. 906–916, 2016.
- [19] C. J. Hardy, R. O. Giaquinto, J. E. Piel, A. Rohling, W. Kenneth, L. Marinelli, D. J. Blezek, E. W. Fiveland, R. D. Darrow, and T. K. Foo, “128-channel body mri with a flexible high-density receiver-coil array,” *Journal of Magnetic Resonance Imaging*, vol. 28, no. 5, pp. 1219–1225, 2008.
- [20] R. F. Lee, R. O. Giaquinto, and C. J. Hardy, “Coupling and decoupling theory and its application to the mri phased array,” *Magnetic resonance in medicine*, vol. 48, no. 1, pp. 203–213, 2002.
- [21] X. Zhang and A. Webb, “Design of a capacitively decoupled transmit/receive nmr phased array for high field microscopy at 14.1 t,” *Journal of Magnetic Resonance*, vol. 170, no. 1, pp. 149–155, 2004.
- [22] B. Wu, X. Zhang, P. Qu, and G. X. Shen, “Capacitively decoupled tunable loop microstrip (tlm) array at 7 t,” *Magnetic resonance imaging*, vol. 25, no. 3, pp. 418–424, 2007.

- [23] B. Guérin, M. Gebhardt, S. Cauley, E. Adalsteinsson, and L. L. Wald, “Local specific absorption rate (sar), global sar, transmitter power, and excitation accuracy trade-offs in low flip-angle parallel transmit pulse design,” *Magnetic Resonance in Medicine*, vol. 71, no. 4, pp. 1446–1457, 2014.
- [24] X. Yan, C. Ma, L. Shi, Y. Zhuo, X. J. Zhou, L. Wei, and R. Xue, “Optimization of an 8-channel loop-array coil for a 7 t mri system with the guidance of a co-simulation approach,” *Applied Magnetic Resonance*, vol. 45, no. 5, pp. 437–449, 2014.
- [25] B. Wu, X. Zhang, P. Qu, and G. X. Shen, “Design of an inductively decoupled microstrip array at 9.4 t,” *Journal of Magnetic Resonance*, vol. 182, no. 1, pp. 126–132, 2006.
- [26] J. Hoffmann, G. Shajan, K. Scheffler, and R. Pohmann, “Numerical and experimental evaluation of rf shimming in the human brain at 9.4 t using a dual-row transmit array,” *Magnetic Resonance Materials in Physics, Biology and Medicine*, vol. 27, no. 5, pp. 373–386, 2014.
- [27] M. Kozlov and R. Turner, “Assessment of decoupling between mri array elements at 300 mhz,” *Session 3P5 Antenna and EMC*, p. 597, 2013.
- [28] J. Tropp, “The theory of the bird-cage resonator,” *Journal of Magnetic Resonance (1969)*, vol. 82, no. 1, pp. 51–62, 1989.
- [29] J. Jin, *Electromagnetic analysis and design in magnetic resonance imaging*, vol. 1. CRC press, 1998.
- [30] E. B. Rosa, *On the geometrical mean distances of rectangular areas and the calculation of self-inductance*, vol. 3. Govt. Print. Off., 1907.
- [31] E. B. Rosa, *The self and mutual inductances of linear conductors*. US Department of Commerce and Labor, Bureau of Standards, 1908.
- [32] F. W. Grover, *Inductance calculations: working formulas and tables*. Courier Corporation, 2004.

- [33] J. Jin and J. Chen, “On the sar and field inhomogeneity of birdcage coils loaded with the human head,” *Magnetic resonance in medicine*, vol. 38, no. 6, pp. 953–963, 1997.
- [34] A. Etminan, A. Sadeghi, and L. Gürel, “Electromagnetic imaging of three-dimensional dielectric objects with newton minimization,” in *Antennas and Propagation Society International Symposium (APSURSI), 2014 IEEE*, pp. 876–877, IEEE, 2014.
- [35] A. Greenbaum, *Iterative methods for solving linear systems*, vol. 17. Siam, 1997.
- [36] T. M. Habashy and A. Abubakar, “A general framework for constraint minimization for the inversion of electromagnetic measurements,” *Progress In Electromagnetics Research*, vol. 46, pp. 265–312, 2004.
- [37] D. M. Pozar, *Microwave engineering*. John Wiley & Sons, 2009.
- [38] C. E. Hayes and M. G. Eash, “Shield for decoupling rf and gradient coils in an nmr apparatus,” Feb. 10 1987. US Patent 4,642,569.
- [39] P. B. Roemer and W. A. Edelstein, “Rf shield for rf coil contained within gradient coils of nmr imaging device,” Oct. 3 1989. US Patent 4,871,969.
- [40] F. Bloch and A. Siegert, “Magnetic resonance for nonrotating fields,” *Physical Review*, vol. 57, no. 6, p. 522, 1940.
- [41] L. I. Sacolick, F. Wiesinger, I. Hancu, and M. W. Vogel, “B1 mapping by bloch-siegert shift,” *Magnetic Resonance in Medicine*, vol. 63, no. 5, pp. 1315–1322, 2010.
- [42] L. Darrasse and G. Kassab, “Quick measurement of nmr-coil sensitivity with a dual-loop probe,” *Review of scientific instruments*, vol. 64, no. 7, pp. 1841–1844, 1993.
- [43] G. Giovannetti, F. Frijia, V. Hartwig, L. Menichetti, D. De Marchi, V. Positano, L. Landini, M. Lombardi, M. F. Santarelli, and J. H. Ardenkjaer-Larsen, “A novel method for coil efficiency estimation: Validation with a

13c birdcage,” *Concepts in Magnetic Resonance Part B: Magnetic Resonance Engineering*, vol. 41, no. 4, pp. 139–143, 2012.

- [44] I. J. Bahl, *Lumped elements for RF and microwave circuits*. Artech house, 2003.
- [45] T. S. Ibrahim, R. Lee, B. A. Baertlein, Y. Yu, and P.-M. L. Robitaille, “Computational analysis of the high pass birdcage resonator: finite difference time domain simulations for high-field mri,” *Magnetic resonance imaging*, vol. 18, no. 7, pp. 835–843, 2000.
- [46] D. Hoult and P. C. Lauterbur, “The sensitivity of the zeugmatographic experiment involving human samples,” *Journal of Magnetic Resonance (1969)*, vol. 34, no. 2, pp. 425–433, 1979.